



RESEARCH ARTICLE

# Label-Free Imaging to Track Reprogramming of Human Somatic Cells

Kaivalya Molugu,<sup>1,2</sup> Giovanni A. Battistini,<sup>2</sup> Tiffany M. Heaster,<sup>3,4</sup> Jacob Rouw,<sup>2,3</sup> Emmanuel C. Guzman,<sup>4</sup> Melissa C. Skala,<sup>3,4,\*</sup> and Krishanu Saha<sup>2,3,\*</sup>

## Abstract

The process of reprogramming patient samples to human-induced pluripotent stem cells (iPSCs) is stochastic, asynchronous, and inefficient, leading to a heterogeneous population of cells. In this study, we track the reprogramming status of patient-derived erythroid progenitor cells (EPCs) at the single-cell level during reprogramming with label-free live-cell imaging of cellular metabolism and nuclear morphometry to identify high-quality iPSCs. EPCs isolated from human peripheral blood of three donors were used for our proof-of-principle study. We found distinct patterns of autofluorescence lifetime for the reduced form of nicotinamide adenine dinucleotide (phosphate) and flavin adenine dinucleotide during reprogramming. Random forest models classified iPSCs with ~95% accuracy, which enabled the successful isolation of iPSC lines from reprogramming cultures. Reprogramming trajectories resolved at the single-cell level indicated significant reprogramming heterogeneity along different branches of cell states. This combination of micropatterning, autofluorescence imaging, and machine learning provides a unique, real-time, and nondestructive method to assess the quality of iPSCs in a biomanufacturing process, which could have downstream impacts in regenerative medicine, cell/gene therapy, and disease modeling.

The derivation of donor-specific induced pluripotent stem cells (iPSCs) from somatic cells through reprogramming generates a unique self-renewing cell source for disease modeling, drug discovery, toxicology, and personalized cell therapies.<sup>1–3</sup> These cells carry the donor's genome, facilitating elucidation of the genetic causes of disease, and are immunologically matched to the donor, facilitating the engraftment of cells derived from iPSCs.<sup>4–6</sup>

With several clinical trials underway,<sup>7</sup> there has been significant progress in developing iPSC-based cell therapies in recent years. However, several challenges remain in the field.<sup>8</sup> First, the derivation of high-quality iPSCs must be efficient, rapid, and cost-effective to ensure that patients receive their treatments in a timely manner with autologous iPSC-derived products. Second, reprogramming to make iPSCs for both allogeneic and autologous cell therapy could benefit from standardized manufacturing processes to overcome the inconsistencies arising from variability in human material sources, reagents, delivery of reprogramming factors, microenvironmental fluctuations, or inherent stochasticity in epigenetic processes underpinning reprogramming.<sup>9</sup>

Typical assays currently used for quality control of good manufacturing practices (GMPs)-grade iPSCs include testing for cell line identity (short tandem repeat analysis, single nucleotide polymorphism analysis, genomic sequencing), genomic instability (G-banding, chromosomal microarray, NanoString technology), pluripotency (marker expression analysis through flow cytometry or immunocytochemistry, embryoid body analysis, teratoma assays, Pluritest™, TaqMan Scorecard™ Assay), and residual expression of reprogramming factors (polymerase chain reaction or immunocytochemistry).<sup>10–13</sup> Each of these methods can be low throughput, labor intensive, time consuming, and require destructive processing.

Nondestructive strategies such as automated machine learning can be used to identify various cell types and structures in cell cultures from bright-field images.<sup>14–18</sup> However, such automated methods to identify iPSCs, in particular, have had limited success in the field.<sup>19–21</sup> Deep learning has recently been employed to analyze monoclonal cell cultures of established iPSC lines,<sup>22</sup> but reprogramming cultures involve a higher number of cell fate transitions that have yet to be analyzed through

<sup>1</sup>Biophysics Graduate Program, University of Wisconsin-Madison, Madison, Wisconsin, USA; <sup>2</sup>Wisconsin Institute for Discovery, University of Wisconsin-Madison, Madison, Wisconsin, USA; <sup>3</sup>Department of Biomedical Engineering, University of Wisconsin-Madison, Madison, Wisconsin, USA; and <sup>4</sup>Morgridge Institute for Research, Madison, Wisconsin, USA.

\*Address correspondence to: Krishanu Saha, Department of Biomedical Engineering and Wisconsin Institute for Discovery, University of Wisconsin-Madison, Madison, WI 53715, USA, E-mail: ksaha@wisc.edu; Melissa Skala, Department of Biomedical Engineering, University of Wisconsin-Madison, and Morgridge Institute for Research, Madison, WI 53715, USA, E-mail: mcskala@wisc.edu

© Kaivalya Molugu et al. 2022; Published by Mary Ann Liebert, Inc. This Open Access article is distributed under the terms of the Creative Commons License [CC-BY] (<http://creativecommons.org/licenses/by/4.0>), which permits unrestricted use, distribution, and reproduction in any medium, provided the original work is properly cited.

deep learning pipelines. Hence, in complex cultures, like those in reprogramming, new standardized platforms with robust analytical methods for identifying high-quality iPSCs are still needed.

Our strategy to identify iPSCs exploits metabolic and nuclear changes during reprogramming. Somatic cells primarily utilize mitochondrial oxidative phosphorylation (OXPHOS) to support cell proliferation,<sup>23</sup> while pluripotent stem cells favor glycolysis in a manner reminiscent of the Warburg effect in cancer cells.<sup>23,24</sup> During reprogramming, somatic cells thus undergo a metabolic shift from OXPHOS to glycolysis,<sup>25,26</sup> accompanied by a transient OXPHOS burst, resulting in the initiation and progression of reprogramming.<sup>27–29</sup>

Recent evidence also indicates that this metabolic shift occurs before changes in gene expression and that the modulation of glycolytic metabolism or OXPHOS alters reprogramming efficiency.<sup>24,30,31</sup> High-resolution imaging of reprogramming cells has also identified that nuclear geometry is dramatically altered during reprogramming.<sup>32–34</sup> Therefore, simultaneous monitoring metabolic and nuclear changes during reprogramming could identify various cell states within reprogramming cultures.

Optical metabolic imaging (OMI) is a noninvasive and label-free two-photon microscopy technique that provides dynamic measurements of cellular metabolism at a single-cell level. OMI is based on the endogenous fluorescence of metabolic coenzymes, reduced form of nicotinamide adenine dinucleotide (NADH) and flavin adenine dinucleotide (FAD),<sup>35</sup> that are both used across several cellular metabolic processes. NADH and reduced form of nicotinamide adenine dinucleotide phosphate (NADPH) have overlapping fluorescence properties and are collectively referred to as reduced form of nicotinamide adenine dinucleotide (phosphate) (NAD(P)H).<sup>36</sup> The optical redox ratio, defined as the ratio of NAD(P)H intensity to the sum of NAD(P)H and FAD intensity, provides a measure of the relative oxidation–reduction state of the cell  $[I_{\text{NAD(P)H}} / (I_{\text{NAD(P)H}} + I_{\text{FAD}})]$ .<sup>37,38</sup>

Fluorescence lifetime imaging microscopy of NAD(P)H and FAD provides additional information specific to protein binding activity. The two-component decays of NAD(P)H and FAD measure the short ( $\tau_1$ ) and long ( $\tau_2$ ) fluorescence lifetimes that correspond to

the free or bound states of these coenzymes,<sup>39–41</sup> along with fractional contributions of short ( $\alpha_1$ ) and long ( $\alpha_2$ ) lifetimes. Since NAD(P)H and FAD are found predominantly in the cytoplasm, the lack of fluorescence signal in images can also be used to identify cell borders and nuclei.<sup>42</sup> Thus, OMI provides multiple readouts for cell metabolism and nuclear morphometry to track metabolic and nuclear changes of cells undergoing reprogramming.

In this study, we address some of the challenges associated with the biomanufacturing of iPSCs by developing a microcontact printed ( $\mu$ CP) platform<sup>34,43,44</sup> to noninvasively monitor metabolic and nuclear changes over 22 days of reprogramming of human erythroid progenitor cells (EPCs) to iPSCs. We demonstrate that OMI is sensitive to the metabolic and nuclear differences during reprogramming, provide accurate identification of reprogramming status of cells using machine learning models, and subsequently build reprogramming trajectories at the single-cell level.<sup>45</sup> Our label-free, nondestructive, rapid, and scalable method to track reprogramming provides novel insights into human cell reprogramming and could enable the development of new technologies for biomanufacturing high-quality iPSCs.

## Results

### Reprogramming on patterned substrates

We first designed a  $\mu$ CP substrate to spatially control the adhesion of EPCs undergoing reprogramming.<sup>34,43,46</sup> The  $\mu$ CP substrate is formed by coating circular regions of 300  $\mu\text{m}$  radius, referred to as  $\mu$ Features, with Matrigel on a 35-mm ibiTreat dish that allows for cell adhesion. The remaining regions of the dish are then back-filled with polycationic graft copolymer, poly(L-lysine)-graft-poly(ethylene glycol) (PLL-g-PEG), that resists protein adsorption and prevents cell adhesion in these regions (Supplementary Fig. S1A).<sup>47,48</sup> The ibiTreat dishes are made of gas-permeable material, enabling maintenance of carbon dioxide or oxygen exchange during cell culture and have high optical quality.

These properties make the dishes suitable for two-photon microscopy during reprogramming. To verify proper coating of the circular  $\mu$ Feature regions, we immunostained for laminin, a

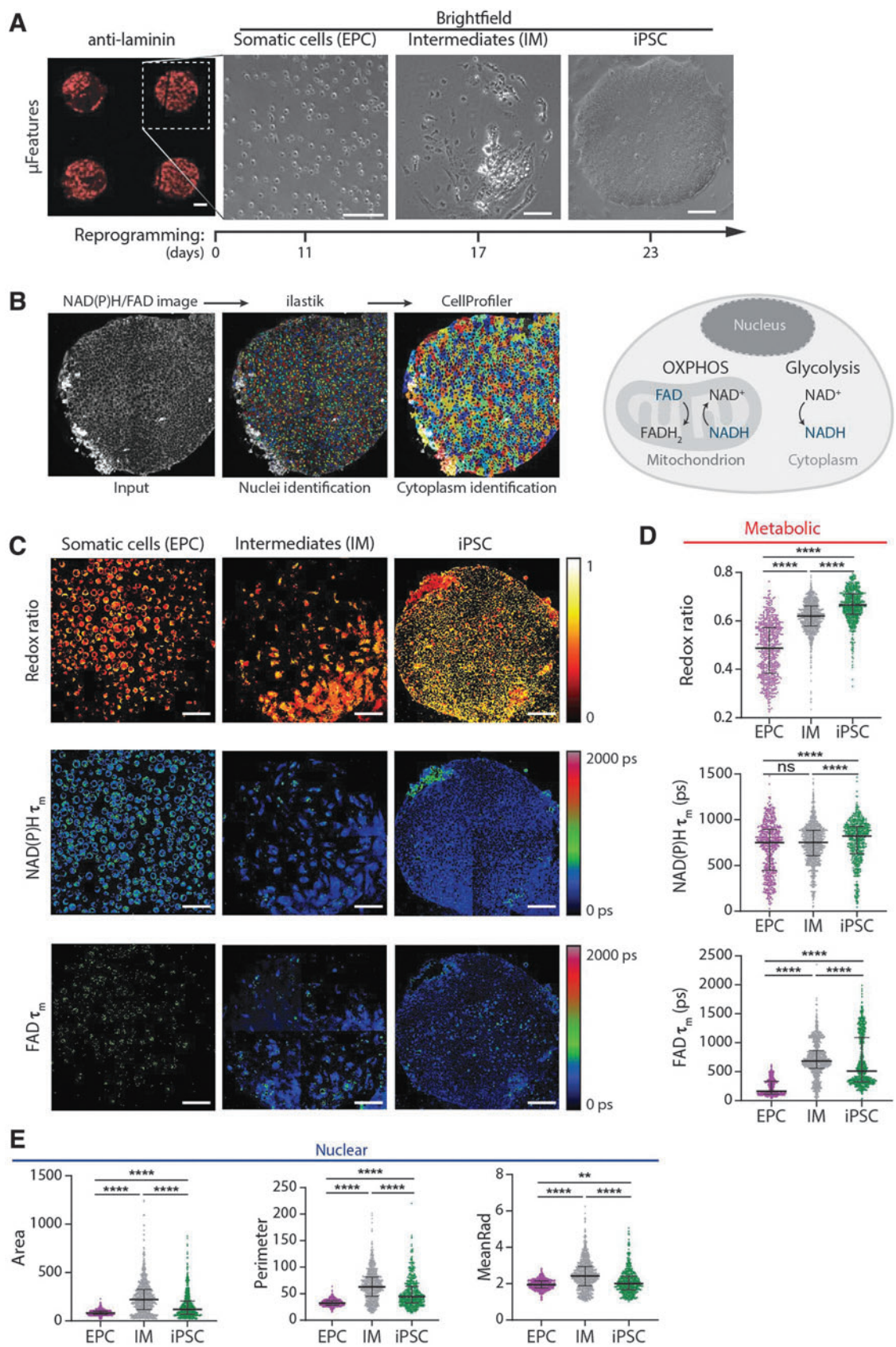
### FIG. 1. NAD(P)H and FAD autofluorescence imaging reveal metabolic differences during reprogramming.

(A) Left: Matrigel-coated  $\mu$ Features on the ibiTreat dish visualized with an anti-laminin antibody (red) show good fidelity in the transfer from the Matrigel-coated polydimethylsiloxane mold. Scale bar, 100  $\mu\text{m}$ . Right: Representative images of the progression of EPCs on a single circular  $\mu$ Feature (300  $\mu\text{m}$  radius) through a reprogramming time course.

(B) Left: Image analysis pipeline to identify metabolic and nuclear parameters using ilastik and CellProfiler software. Right: Schematic representation of cell metabolism with NADH and FAD highlighted as the fluorescent molecules in the diagram, and molecules in bold indicate the net direction of the reaction.

(C) Representative optical redox ratio, NAD(P)H  $\tau_m$ , and FAD  $\tau_m$  images (3  $\mu$ Features selected from 36  $\mu$ Features acquired from three different donors) for EPC, IM, and iPSC. Color bars indicated on the right are a representation of the values optical redox ratio, NAD(P)H  $\tau_m$ , and FAD  $\tau_m$ . Scale bar, 100  $\mu\text{m}$ .

Single-cell quantitative analysis of (D) metabolic parameters: optical redox ratio, NAD(P)H  $\tau_m$ , FAD  $\tau_m$ ; (E) nuclear parameters: area, perimeter, and mean radius ( $n=561, 990, \text{ and } 586$  for EPC, IM, and iPSC, respectively). Data are presented as median with interquartile range for each cell type. Statistical significance was determined by one-way ANOVA using the Kruskal–Wallis test for multiple comparisons; ns for  $p \geq 0.05$ , \* for  $p < 0.05$ , \*\* for  $p < 0.01$ , \*\*\* for  $p < 0.001$ , \*\*\*\* for  $p < 0.0001$ . ANOVA, analysis of variance; EPC, erythroid progenitor cells; FAD, flavin adenine dinucleotide; IM, intermediate; iPSC, induced pluripotent stem cell; NADH, reduced form of nicotinamide adenine dinucleotide; NAD(P)H, reduced form of nicotinamide adenine dinucleotide (phosphate); ns, nonsignificant.



major component of Matrigel.<sup>49</sup> Fluorescence imaging showed laminin consistently within the circular  $\mu$ Features indicating uniform patterning of Matrigel (Fig. 1A; left). We next assessed the ability of the  $\mu$ CP substrates to enable cell attachment by seeding two different cell types: human dermal fibroblasts (HDFs) and human embryonic stem cells (hESCs). We observed that both HDFs and hESCs remained viable, attached, and confined to the circular  $\mu$ Features indicating that the  $\mu$ CP substrates enable spatial control of cell adhesion (Supplementary Fig. S1B).

Next, peripheral blood mononuclear cells (PBMCs) were isolated from healthy human donors and further enriched for EPCs before the delivery of reprogramming factors. We examined the enrichment of EPCs by flow cytometry with erythroid cell surface marker CD71.<sup>50</sup> Flow cytometry confirmed the presence of enriched EPCs showing that >98% of the cells expressed CD71 on day 10 of PBMC culture (Supplementary Fig. S1C).

To initiate reprogramming, we electroporated EPCs with four episomal reprogramming plasmids<sup>51,52</sup>—encoding OCT4, shRNA knockdown of p53, SOX2, KLF4, L-MYC, LIN28, and miR302–367 cluster—and seeded them onto  $\mu$ CP substrates. We assessed the ability of the  $\mu$ CP substrates to sustain long-term reprogramming studies by performing high-content imaging to track individual  $\mu$ Features (>30  $\mu$ Features per 35-mm dish) longitudinally at multiple time points over the ~3 weeks of reprogramming time course. Day 22 was chosen as the reprogramming endpoint because there were several  $\mu$ Features with at least one iPSC colony at this time point without significant outgrowth beyond the boundaries of the  $\mu$ Features.

Although the starting EPCs (day 0) are nonadherent, EPCs undergoing reprogramming start adhering to the  $\mu$ CP substrates on day 8. Cells in the middle of reprogramming (day 8–day 17) that lack EPC markers or iPSC markers are broadly termed as intermediates (IMs), consistent with prior nomenclature in the field.<sup>53</sup> Moreover, endpoint iPSCs on day 22 remain adhered to the  $\mu$ CP substrates within each circular  $\mu$ Feature (Fig. 1A; right), indicating that  $\mu$ CP substrates can support the full reprogramming of EPCs. Overall, the  $\mu$ CP platform provides unique spatial control over cells and enables high-content quantitative imaging of reprogramming.

### OMI reveals metabolic states during reprogramming

Cellular metabolism plays an important role in regulating reprogramming and pluripotency of iPSCs,<sup>54–58</sup> and can be non-invasively monitored through OMI. NAD(P)H is an electron donor and FAD is an electron acceptor. Both are present in all cells as coenzymes and provide energy for metabolic reactions. For example, glycolysis in the cytoplasm generates NADH and pyruvate, whereas OXPHOS consumes NADH and produces FAD (Fig. 1B; right). Autofluorescence imaging of NAD(P)H and FAD can thus detect the oxidation–reduction state of a cell and is influenced by many biochemical reactions.<sup>35,59</sup>

We tracked the autofluorescence dynamics of NAD(P)H and FAD by performing OMI on cells attached to  $\mu$ CP substrates at different time points during EPC reprogramming. In these images, the nucleus remains dark as NAD(P)H is primarily located in cytosol and mitochondria, and FAD is primarily located in mitochondria. The NAD(P)H images were used as inputs for an image

analysis software, ilastik,<sup>60</sup> to identify the nuclei. The identified nuclei were then used as an input for a high-content image analysis pipeline in CellProfiler software<sup>61</sup> to segment the cytoplasm, and measure various metabolic and nuclear parameters (Fig. 1B; left).

Altogether, 11 metabolic parameters (NAD(P)H intensity,  $I_{\text{NAD(P)H}}$ ; NAD(P)H  $\alpha_1$ ; NAD(P)H  $\tau_1$ ; NAD(P)H  $\tau_2$ ; NAD(P)H mean lifetime,  $\tau_m = \alpha_1\tau_1 + \alpha_2\tau_2$ ; FAD intensity,  $I_{\text{FAD}}$ ; FAD  $\alpha_1$ ; FAD  $\tau_1$ ; FAD  $\tau_2$ ; FAD  $\tau_m$ ; optical redox ratio,  $I_{\text{NAD(P)H}}/[I_{\text{NAD(P)H}} + I_{\text{FAD}}]$ ) and 8 nuclear parameters<sup>34</sup> (area; perimeter; mean radius [MeanRad]; nuclear shape index [NSI]; solidity; extent; number of neighbors [#Neigh]; distance to closest neighbor [1stNeigh]) were measured by the analysis pipeline. Supplementary Figure S1D provides further details of each parameter.

By fixing the cultures at these time points, we verified the cell type by immunofluorescent staining: EPCs (CD71<sup>+</sup>, Nanog<sup>-</sup>), IMs (CD71<sup>-</sup>, Nanog<sup>-</sup>), and iPSCs (CD71<sup>-</sup>, Nanog<sup>+</sup>) (Supplementary Fig. S1E). NAD(P)H and FAD autofluorescence imaging revealed metabolic differences between starting EPCs, IMs, and iPSCs (Supplementary Figs. S2 and S3).

We observed a significant increase in the optical redox ratio (iPSC>IM>EPC) during reprogramming (Fig. 1C), indicating that individual EPCs are more oxidized than individual IMs and iPSCs (Fig. 1D). In addition, we noted that patterned IMs and iPSCs have significantly higher optical redox ratios than their nonpatterned counterparts (Supplementary Fig. S2K). This observation is consistent with previous studies that show that mechanical cues can regulate their relative use of glycolysis.<sup>62–65</sup>

Next, we observed that NAD(P)H and FAD lifetime components undergo biphasic changes during the progress of reprogramming. FAD lifetime components undergo a more significant and pronounced change relative to the NAD(P)H components (Fig. 1D and Supplementary Fig. S2A–J). On average, the fraction of protein-bound FAD (FAD  $\alpha_1$ ) first decreases from its levels in EPCs to those in IMs and then increases during the IM to iPSC transition, which could be reflective of the OXPHOS burst (Supplementary Fig. S2H).<sup>27–29</sup> FAD  $\tau_m$  (Fig. 1D) is inversely related to FAD  $\alpha_1$  and, therefore, undergoes a biphasic change that is opposite to that of FAD  $\alpha_1$  (Supplementary Fig. S2H). Similar biphasic changes occur in nuclear parameters during reprogramming, which is consistent with our previous study (Fig. 1E and Supplementary Fig. S3).<sup>34</sup>

We compared these measurements on cells undergoing reprogramming to established cell lines and primary cell populations. Both pluripotent stem cell lines—established hESCs and iPSC lines—have similar values for most metabolic and nuclear parameters, as expected. The significant differences observed between hESCs and iPSCs in some metabolic and nuclear parameters (Supplementary Figs. S2 and S3) may be because iPSCs have not undergone any passages in contrast to the hESC line.<sup>24</sup>

Fibroblasts from human donors (HDFs) had metabolic parameters significantly different from those of EPCs (Supplementary Fig. S2). This difference could be because (1) fibroblasts are adherent whereas starting EPCs are nonadherent and (2) fibroblasts and EPCs have different proliferation rates and energy needs. Taken together, autofluorescence imaging of NAD(P)H and FAD revealed significant dynamic changes for various cell populations during reprogramming.

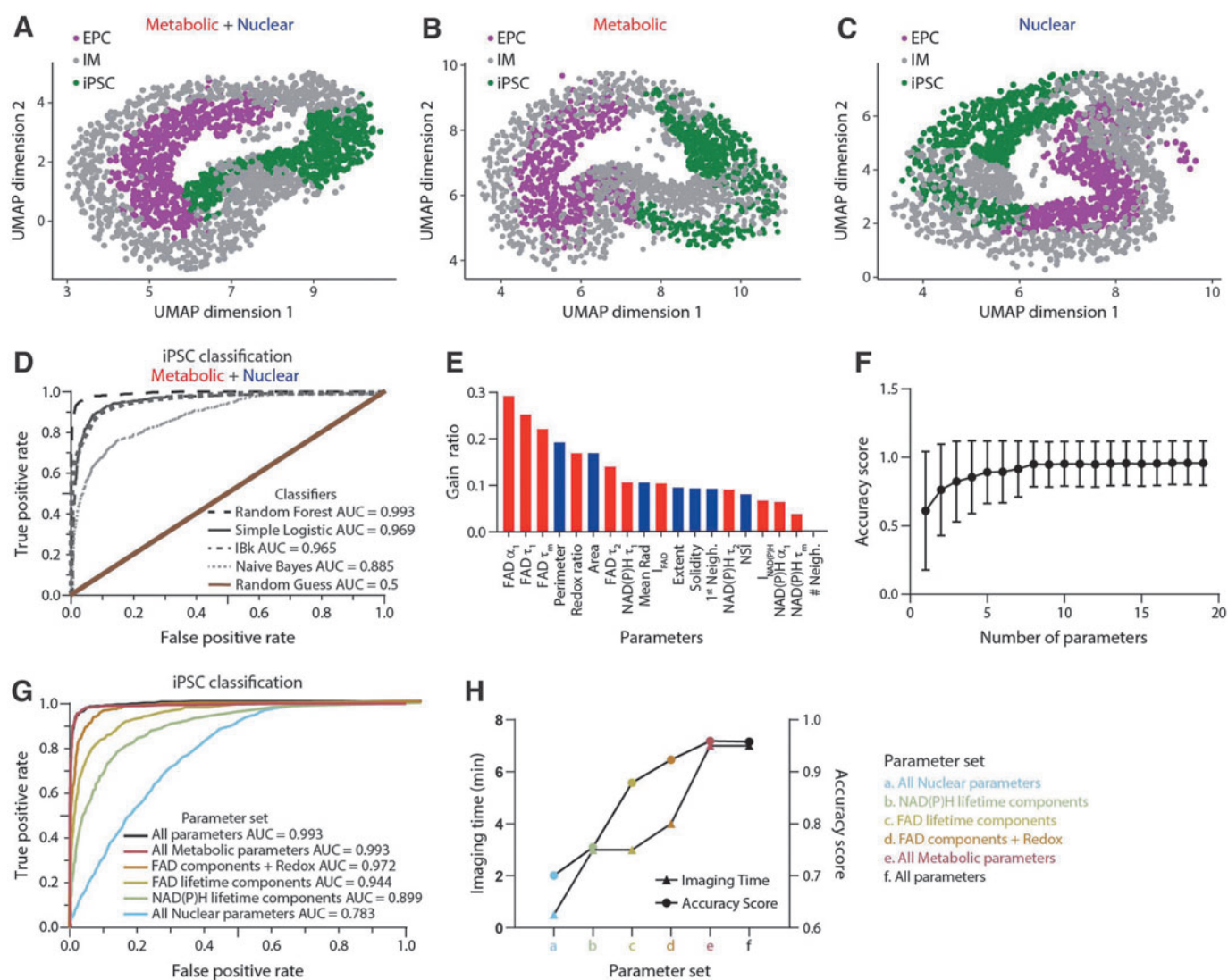


**FIG. 2. Optical metabolic imaging enables the classification of cells based on their reprogramming status.**

UMAP dimensionality reduction was performed on **(A)** all 11 metabolic and 8 nuclear parameters, **(B)** only 11 metabolic parameters, and **(C)** only 8 nuclear parameters for each cell, projected onto two-dimensional space and enables separation of different cell types (EPC, IM, and iPSC). Each color corresponds to a different cell type. Data are from three different donors. Each dot represents a single cell, and  $n = 561, 990$ , and 586 cells for EPC, IM, and iPSC, respectively.

**(D)** Model performance of the different classifiers (random forest, simple logistic, k-nearest neighbor [IBk], naive Bayes) for iPSCs was evaluated by ROC curves using all 11 metabolic and 8 nuclear parameters. The AUC is provided for each classifier as indicated in the legend.

**(E)** Parameter weights for random forest classification of EPCs, IMs, and iPSCs using the gain ratio method. Analysis was performed at a single-cell level using three different donors.

**(F)** Classification accuracy with respect to number of parameters was evaluated based on the gain ratio parameter selection with the random forest model (parameters added from highest to lowest gain ratio in **(E)**). The number of parameters included in the random forest model is indicated on the x-axis.

**(G)** Model performance of the random forest classifier for iPSCs was evaluated by ROC curves using different metabolic and nuclear parameter combinations as labeled. AUC is provided for each parameter combination as indicated in the legend.

**(H)** Imaging time (left y-axis) and accuracy score (right y-axis) evaluation of the random forest classifier for different metabolic and nuclear parameter combinations as labeled. AUC, area under the curve; OMI, optical metabolic imaging; ROC, receiver operating characteristic; UMAP, Uniform Manifold Approximation and Projection.

**OMI enables the identification of iPSCs with high accuracy**

To visualize cell states within the entire metabolic and nuclear morphometry data set, Uniform Manifold Approximation and Projection (UMAP)<sup>66</sup> was employed on the multidimensional measurements already described. Neighbors were defined through the Jaccard similarity coefficient computed across the metabolic and nuclear parameters. UMAP was chosen over t-distributed stochastic neighbor embedding (t-SNE) since UMAP (Fig. 2A) yielded more distinct clusters for two different known cell types—EPCs and iPSCs—than t-SNE (Supplementary Fig. S4A). Furthermore, the UMAP algorithm took less time than the t-SNE algorithm to implement with our data set. In addition, UMAP can include nonmetric distance functions while preserving the global structure of the data.

UMAP was next used to visualize subsets of the entire data set to investigate which measurements were associated with different cell states. Distinct cell populations could be derived from data sets built exclusively from the 11 metabolic parameters (Fig. 2B) and data sets built exclusively from the 8 nuclear parameters (Fig. 2C). Although these UMAP representations revealed some distinct clusters of EPCs, IMs, and iPSCs, the UMAP generated using both metabolic and nuclear parameters displayed less overlap of cell clusters among EPCs, IMs, and iPSCs (Fig. 2A).

We also plotted a heatmap representation of the z-score of metabolic and nuclear parameters at the donor level (each row is the mean of a single donor and cell type) to examine heterogeneity arising from individual donors (Supplementary Fig. S4B). Despite some donor-to-donor heterogeneity, EPCs and iPSCs could be distinguished visually (Fig. 2A) based on a combination of 11 metabolic and 8 nuclear parameters.

Next, classification models were developed based on 11 metabolic and 8 nuclear parameters to predict the reprogramming status of cells, that is, as either EPCs, IMs, or iPSCs. Supervised machine learning classification (naive Bayes, K-nearest neighbor) and regression algorithms (logistic regression and random forest)<sup>67</sup> were implemented to test the prediction accuracy for iPSCs properly when all the metabolic and nuclear parameters are used. To protect against overfitting, various classification methods were trained using 15-fold cross-validation on single-cell data from three different donors with reprogramming status assigned based on morphological characteristics.

Furthermore, we tested the various classification methods on data collected from CD71 and Nanog immunofluorescence staining with the same cells from three donors (completely independent and nonoverlapping observations). Receiver operating characteristic (ROC; one-vs-rest) curves of the test data revealed highest classification accuracy for predicting iPSCs (area under the curve, AUC=0.993), IMs (AUC=0.993), and EPCs (AUC=0.999) when a random forest model was used (Fig. 2D and Supplementary Fig. S4C, D). We thus used the random forest classification model for further analysis in this study.

Gain ratio analysis on the decision tree within this random forest model revealed that FAD lifetime components, FAD  $\alpha_1$ , FAD  $\tau_1$ , and FAD  $\tau_m$ , are the most important parameters for classifying the reprogramming status of cells (Fig. 2E). This result is consistent with the observation that FAD lifetime components are significantly different among EPCs, IMs, and iPSCs (Fig. 1 and Supplementary Fig. S2). We then plotted the accuracy score as a function of the number of parameters, wherein the parameters with highest gain ratio values (Fig. 2E) were chosen (one parameter means FAD $\alpha_1$ ; two parameters means FAD $\alpha_1$ , FAD $\tau_1$ , and so on).

This plot revealed that the accuracy score increases with the number of parameters until eight parameters (FAD $\alpha_1$ , FAD $\tau_1$ , FAD $\tau_m$ , perimeter, redox ratio, area, FAD $\tau_2$ , NAD(P)H $\tau_1$ ) and plateaus thereafter (Fig. 2F). Notably, high classification accuracy can be achieved for predicting iPSCs (AUC=0.944), IMs (AUC=0.968), and EPCs (AUC=0.987) when using only FAD lifetime variables (FAD  $\tau_m$ ,  $\tau_1$ ,  $\tau_2$ ,  $\alpha_1$ ; collected in the FAD channel alone) (Fig. 2G and Supplementary Fig. S4E, F).

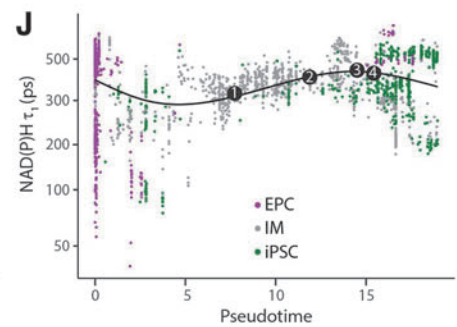
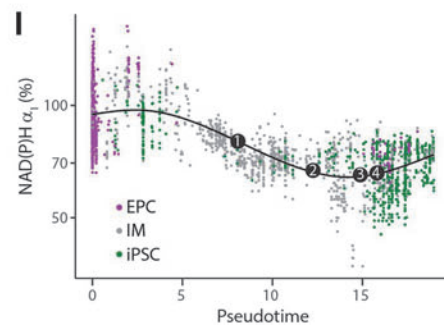
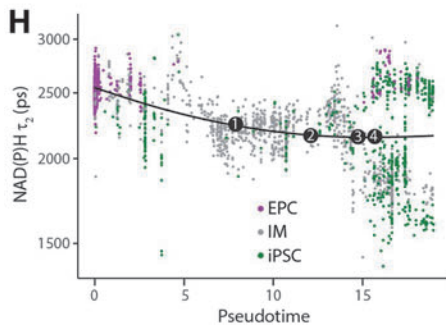
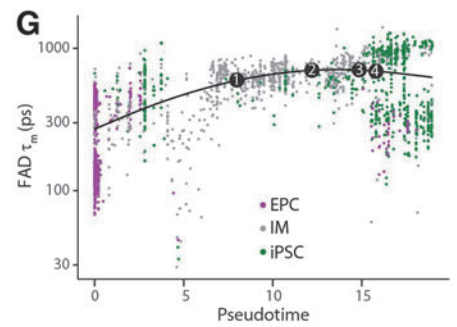
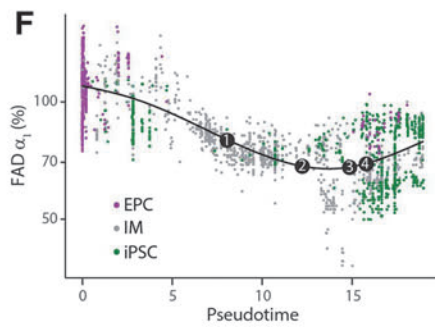
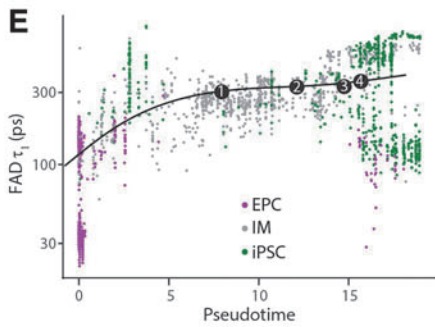
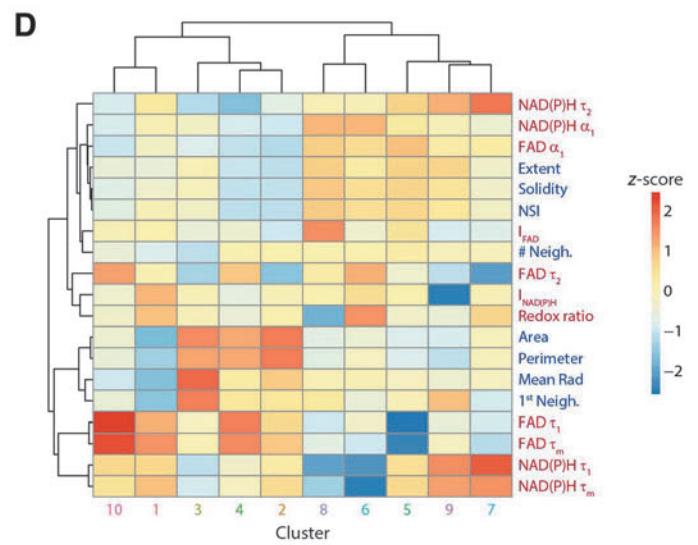
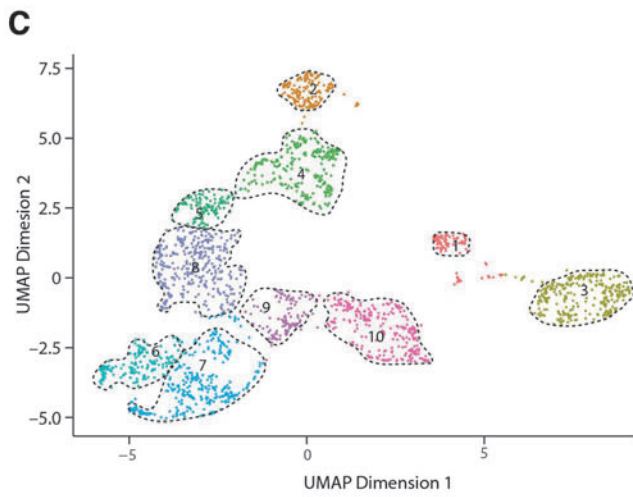
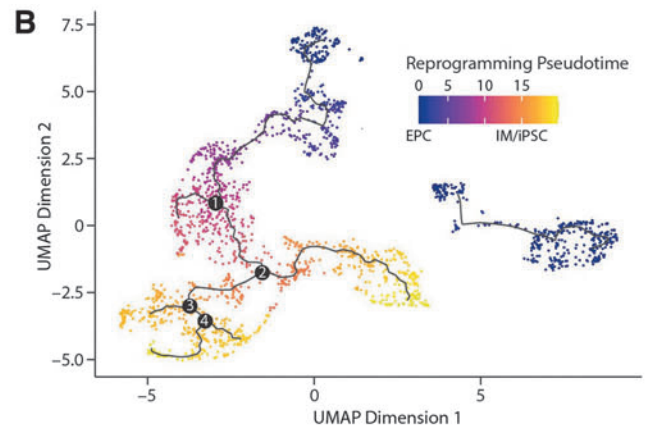
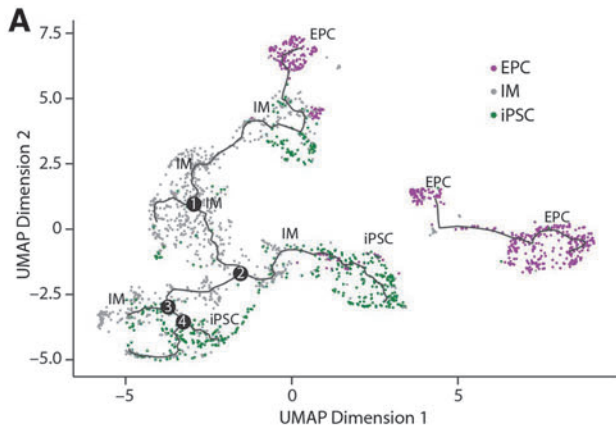
Imaging using only FAD lifetime parameters requires a minimal time of 2.5 min per  $\mu$ Feature (Fig. 2H) without relying on intensity parameters that are associated with higher variability. Such variability can arise from confounding factors associated with intensity levels, such as laser power and detector gain. Hence, FAD lifetime parameters alone are sufficient to classify accurately the reprogramming status of cells.

**Pseudotemporal ordering of single cells resolves cellular transitions**

By sampling a process over a time course, profiles at a single-cell level can be used to order cells along a “pseudotemporal” continuum. Such ordering can resolve cellular transitions during

**FIG. 3. Inference of reprogramming trajectories at the single-cell level reveals heterogeneity during reprogramming.**

Trajectory analysis of reprogramming EPCs constructed from the metabolic and nuclear parameters based on UMAP dimension reduction using Monocle3 revealed four branch points, colored by (A) cell type and (B) pseudotime. (C) Monocle UMAP plots showing clustering of reprogramming EPCs. Samples were grouped into 10 clusters. Cells colored by cluster. (D) Heatmap representing the metabolic and nuclear parameters of 10 clusters. Each column is a separate cell group based on the generated clusters, and each row represents a single metabolic or nuclear parameter. Z-score =  $(\mu_{\text{observed}} - \mu_{\text{row}}) / \sigma_{\text{row}}$ , where  $\mu_{\text{observed}}$  is the mean value of each parameter for each cell;  $\mu_{\text{row}}$  is the mean value of each parameter for all cells together, and  $\sigma_{\text{row}}$  is the standard deviation of each parameter across all cells. Dot plots indicating the expression of (E) FAD  $\tau_1$ , (F) FAD  $\alpha_1$ , (G) FAD  $\tau_m$ , (H) NAD(P)H  $\tau_2$ , (I) NAD(P)H  $\alpha_1$ , and (J) NAD(P)H  $\tau_2$  along the pseudotime. Smooth lines are composed of multiple dots representing the mean expression level at each pseudotime, regardless of the cell type. Four branch points are labeled on the smooth lines.



complex processes such as organismal development.<sup>45,68</sup> Here we used 11 metabolic and 8 nuclear parameters to construct pseudotime trajectories of cellular reprogramming at a single-cell level using the Monocle3 algorithm.<sup>45,69</sup> Monocle3 is a trajectory inference method that learns combinatorial changes that each cell must go through as a part of a process and subsequently places each cell at its inferred location in the trajectory.

The inferred pseudotime trajectories built on our entire data set consisted of EPCs, IMs, and iPSCs distributed across 10 clusters, 4 branching events, and 1 disconnected branch (Fig. 3A–C). The primary trajectory—colored by pseudotime and actual reprogramming time points—exhibited transitions from EPCs to IMs to iPSCs as expected (Fig. 3B and Supplementary Fig. S5A).

Trajectory inference indicated that the starting EPCs were heterogeneous and occupied three clusters (Fig. 3C; clusters: 1, 2, and 3). Although cluster 2 consists of starting EPCs that undergo reprogramming, clusters 1 and 3 constituted the disconnected branch with EPCs that failed to progress through reprogramming. iPSCs predominantly occupied two clusters (clusters 7 and 10) irrespective of the reprogramming time point, whereas IMs belonged to several clusters (clusters 4, 5, 6, 8, and 9) with clusters 6 and 8 concentrated at the unsuccessful reprogramming branches (Fig. 3C).

Overall, these various trajectories provide a detailed map of several cases of reprogramming heterogeneity within human cells. For example, cells that advance right at branch points 1, 2, and 3 (Fig. 3A, B) completely reprogram to iPSCs within 25 days while cells that proceed left at branch points 1 and 3 (Fig. 3A, B) remain as IMs.

Cellular clusters that are adjacent to each other on the reprogramming pseudotime axis exhibit high correlation in their parameter values: that is, EPCs (cluster: 2) have a high correlation with early IMs (cluster: 4), whereas late IMs (clusters: 5, 6, 8, and 9) demonstrate high correlation with iPSCs (cluster: 7) (Fig. 3D). Moderate correlation of cells (cluster: 10) with the starting EPC cluster 1 could indicate more incompletely or partially reprogrammed cells in cluster 10 relative to the iPSCs in cluster 7. When we compared IMs that undergo reprogramming (clus-

ter: 9) and the IMs that do not reprogram to iPSCs (cluster: 6), we noted differences in their NAD(P)H lifetime components, indicating that these parameters might play a role in identifying reprogramming cell fate.

To further examine the parameters that distinguished the cell clusters, we performed another correlation analysis using Moran's I,<sup>70</sup> which is a statistic that reports whether cells at nearby positions on a trajectory will have similar (or dissimilar) expression levels for a given parameter (Supplementary Fig. S5B). When the parameters were ranked by Moran's I, FAD lifetime parameters (FAD  $\tau_1$ ,  $\tau_2$ ,  $\tau_m$ ) were most important in distinguishing clusters followed by NAD(P)H lifetime parameters (NAD(P)H  $\tau_2$ ,  $\alpha_1$ ,  $\tau_1$ ), in agreement with expression level maps (Supplementary Fig. S5C–H).

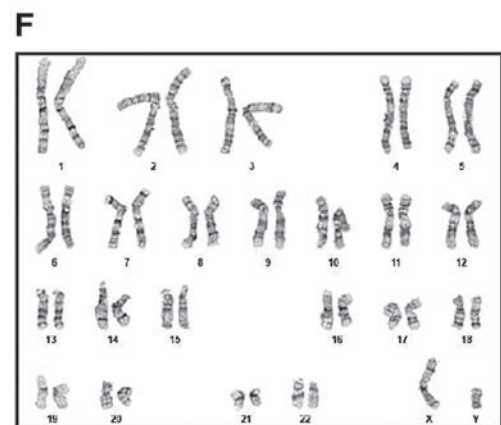
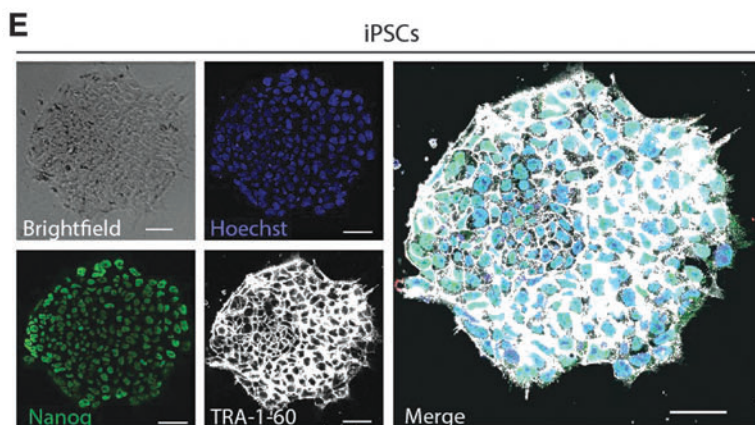
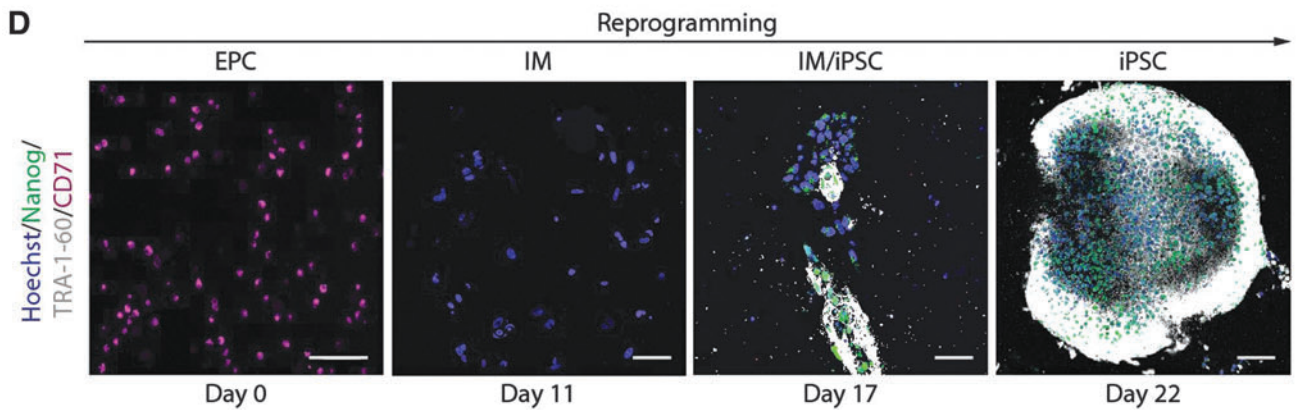
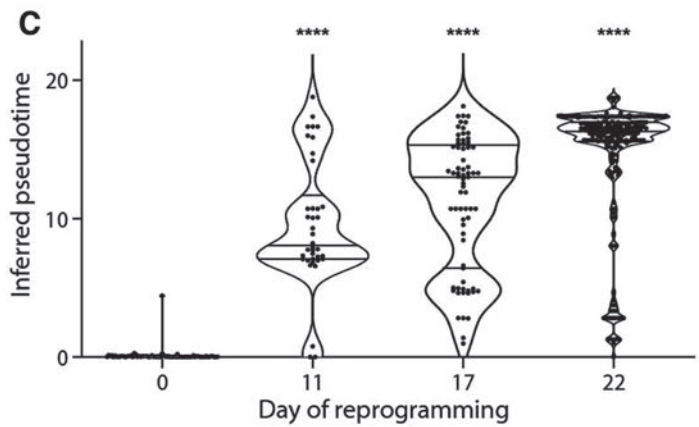
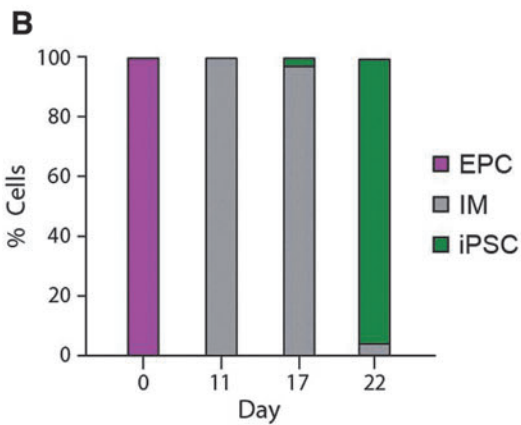
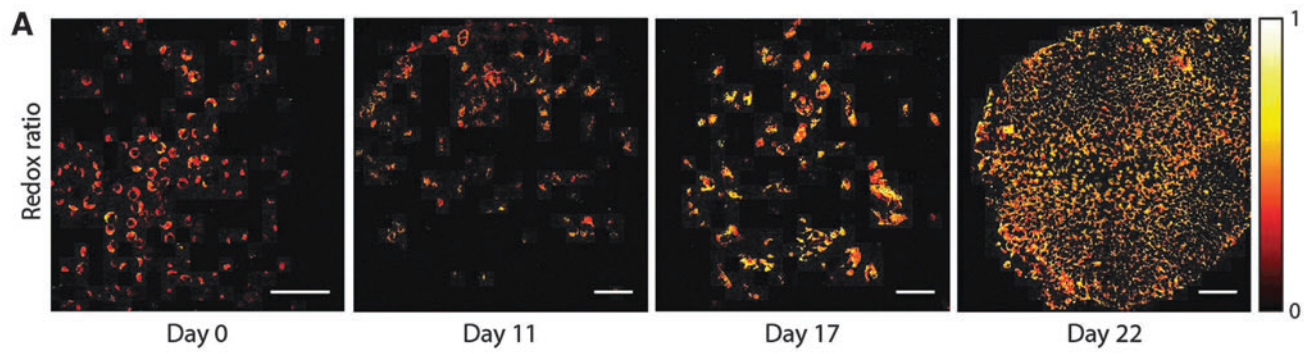
This result is consistent with high gain ratio values for FAD lifetime parameters (Fig. 2E) and the observation FAD lifetime parameters are significantly different among EPCs, IMs, and iPSCs (Fig. 1D). When we plotted the identified important metabolic parameters as a function of pseudotime, we observed that they undergo biphasic changes during reprogramming that could be representative of the OXPHOS burst (Fig. 3E–J). These pseudotime trajectories complement the UMAP visualizations (Fig. 2A–C) by providing higher temporal resolution of changes occurring during reprogramming.

### Isolation of high-quality iPSCs

Although visualizing reprogramming heterogeneity at a high temporal resolution and single-cell resolution with our methods can be insightful, the terminal goal of any reprogramming platform is to successfully isolate iPSCs that can be used for downstream applications. As proof of concept, we used a combination of OMI,  $\mu$ CP platform, and machine learning models developed in this study to isolate high-quality iPSCs (Fig. 4). First, we tracked the metabolic and nuclear parameters of  $\mu$ Features throughout the reprogramming time course using OMI (Fig. 4A). Second, we employed our random forest classification model to predict the reprogramming status of the tracked  $\mu$ Features (Fig. 4B).

## FIG. 4. *In situ* OMI of $\mu$ Features aids in the identification and isolation of iPSCs.

- (A) Representative optical redox ratio images of a single  $\mu$ Feature at different days through the reprogramming time course. Color bar is indicated on the right. Scale bar, 100  $\mu$ m.
- (B) Stacked column bar graph showing the variation in distribution of cell types during reprogramming as classified by the random forest model using all metabolic and nuclear parameters. The color of the bar corresponds to the cell type and the height of the bar represents the percentage of the cell type.
- (C) Violin plots showing the distribution of reprogramming pseudotime of single cells within a  $\mu$ Feature as a function of the actual reprogramming time point. Middle solid line indicates median and upper, and bottom solid lines indicate the interquartile range. Statistical significance was determined by one-way ANOVA using the Kruskal–Wallis test for multiple comparisons; ns for  $p \geq 0.05$ , \* for  $p < 0.05$ , \*\* for  $p < 0.01$ , \*\*\* for  $p < 0.001$ , \*\*\*\* for  $p < 0.0001$ .
- (D) Representative images of cell subpopulations on  $\mu$ Features at different days through the reprogramming time course, stained with Hoechst (blue), TRA-1-60 (white), Nanog (green), and CD71 (magenta). Scale bar, 100  $\mu$ m.
- (E) Representative image of iPSC colony isolated from a  $\mu$ Feature, stained with Hoechst (nuclear dye), TRA-1-60, and Nanog (pluripotency markers). Scale bar, 50  $\mu$ m.
- (F) iPSCs derived from  $\mu$ CP substrates show normal karyotypes suggesting that no major chromosome abnormality was present within the cells after reprogramming.



Third, we inferred the pseudotimes during the reprogramming time course to monitor the progress of the  $\mu$ Features along the reprogramming trajectory (Fig. 4C). Finally, we performed immunostaining on the  $\mu$ Features. The reprogramming status predictions made by the machine learning models correlated well with the cell markers detected by immunostaining (Fig. 4D).

Finally, we isolated iPSCs from the  $\mu$ CP culture platform based on the predictions made by the random forest classification model. The physical separation of  $\mu$ Features from one another, combined with a high fraction of predicted iPSCs, even up to 100% throughout the  $\mu$ Feature, resulted in easy picking and isolation of iPSCs. We further confirmed that the isolated iPSC lines expressed pluripotency markers (Fig. 4E) and showed no genomic abnormalities (Fig. 4F), indicating that our approach supports the generation of genetically stable iPSC lines.

## Discussion

In this study, we report a noninvasive, high-throughput, quantitative, and label-free imaging platform to predict the reprogramming outcome of EPCs by combining micropatterning, live-cell autofluorescence imaging, and automated machine learning. We can predict the reprogramming status of EPCs at any time point during reprogramming with an accuracy of  $\sim 95\%$  and model performance of  $\sim 0.99$  (AUC of ROC) using a random forest classification model with 11 metabolic parameters and 8 nuclear parameters (Fig. 2G and Supplementary Fig. S4C–F). In addition, we provide a single-cell roadmap of EPC reprogramming, which reveals diverse cell fate trajectories of individual reprogramming cells (Fig. 3).

Recent evidence indicates that metabolic changes during reprogramming include decreasing OXPHOS and increasing glycolysis,<sup>26,71</sup> along with a transient hyperenergetic metabolic state, called OXPHOS burst. This OXPHOS burst occurs at an early stage of reprogramming and shows characteristics of both high OXPHOS and high glycolysis, which could be a regulatory cue for the overall shift of reprogramming.<sup>28,29,72,73</sup> These changes are accompanied by alterations in the amounts of corresponding metabolites and have been confirmed by genome-wide analyses of gene expression, protein levels, and metabolomic profiling.<sup>53,74–76</sup>

The shifts in cellular metabolism affect enzymes that control epigenetic configuration,<sup>77</sup> which can impact chromatin reorganization and provide a basis for changes in nuclear morphology as well as gene expression during reprogramming.<sup>34,78–81</sup> Consistent with these studies, the redox ratio increases during reprogramming (Fig. 1D), which could be indicative of increased glycolysis during reprogramming.<sup>82</sup>

The changes in NAD(P)H and FAD lifetime parameters that occur during reprogramming (Fig. 1 and Supplementary Fig. S2) could reflect changes in quencher concentrations, such as oxygen, tyrosine, or tryptophan, or changes in local temperature and pH.<sup>35,83,84</sup> Specifically, the biphasic changes in the metabolic and nuclear parameters could be due to the increased production of reactive oxygen species (ROS) by mito-

chondria<sup>35,59,85,86</sup> during the OXPHOS burst. The generated ROS could further serve as a signal to activate nuclear factor (erythroid derived 2)-like-2 (NRF-2), which then induces hypoxia-inducible factors (HIFs) that promote glycolysis during reprogramming by increasing the expression levels of the glycolysis-related genes.<sup>25,73,75</sup>

Moreover, the importance of FAD parameters for distinguishing various reprogramming cell types (Figs. 1D and 2E) could point to the significant changes in the mitochondrial environment during reprogramming. The differences in NAD(P)H lifetime parameters among IMs that successfully undergo reprogramming and those that do not (Fig. 3D) may suggest a role for molecular pathways involving NAD(P)H in impacting reprogramming barriers and thus the end cell fate of reprogramming cells.

The classification models trained on all 11 metabolic and 8 nuclear parameters had the highest accuracy. Random forest models using only FAD lifetime parameters, in particular, yielded comparatively high ROC AUC values (Fig. 2G and Supplementary Fig. S4E, F). In addition, FAD lifetime parameters were more accurate for predicting reprogramming status than using nuclear parameters alone, which can be obtained using wide-field or confocal fluorescence microscopy.

Imaging only FAD lifetime parameters instead of imaging all the parameters significantly reduced the time of imaging from 7 to 2.5 min per  $\mu$ Feature (Fig. 2H). This reduction in imaging time is especially helpful when assessing multiple  $\mu$ Features for iPSC quality at larger scales, and lifetime measurements benefit from fewer confounding factors and less variability compared with intensity measurements.

Prior studies on the heterogeneity of reprogramming relied on bulk analysis<sup>87–90</sup> or single-cell analysis<sup>91–99</sup> techniques. Prior bulk analyses encountered challenges in characterizing the variability in both the starting cell population and during fate conversion, owing to the variable kinetics and low efficiency of reprogramming, and single-cell techniques disrupted the cellular microenvironment, resulting in significant changes in the biophysical properties of cells undergoing reprogramming. Our methods overcome these challenges with the combination of a  $\mu$ CP culture platform, OMI, and machine learning.

First, the  $\mu$ CP platform dissects cell cultures undergoing reprogramming into hundreds of cell subpopulations that enables easy tracking of cells undergoing reprogramming with imaging time as low as 2.5 min per  $\mu$ Feature. Circular and isolated  $\mu$ Features, however, are not necessary to implement OMI. Moreover, the  $\mu$ CP platform ensures an intact microenvironment for reprogramming cells while enabling single-cell analysis. Second, OMI provides single-cell measurements nondestructively to assess the influence of neighboring cells and provides high temporal resolution for time-course studies of reprogramming. Finally, machine learning with trajectory inference is applied here to a new type of cellular measurement, single cell metabolism. These methods excel in analyzing time course data containing asynchronous processes within cells—as seen in prior studies with flow cytometry and gene expression data.<sup>45,74,97,98,100</sup> Machine learning here overcomes the problems of reprogramming trajectories built based on absolute

time points. Overall, these methods could aid in the identification of somatic cells or early reprogramming cells that are refractory toward reprogramming and thus increase the success rate of iPSC generation from patient-derived primary cells.

Our methods could be adapted for industrial-scale GMP-compliant manufacturing system. First, the  $\mu$ CP platform involves direct extracellular matrix printing onto optically clear substrates (Supplementary Fig. S1A) and does not involve any gold coating, unlike traditional microcontact printing methods.<sup>101,102</sup> Therefore, the  $\mu$ CP platform is cost-effective and relatively simple because it does not require cleanroom access. Plus, our  $\mu$ CP platform utilizes prior advances in the field with xeno-free and feeder-free medium, thus preventing reprogramming inconsistencies arising from the undefined nature of xeno components. Second, we used EPCs isolated from peripheral blood as the starting cell type for reprogramming due to their lack of genomic rearrangements and demonstrated reprogramming ability.<sup>103,104</sup> Moreover, peripheral blood collection is a routine laboratory procedure. The use of EPCs with episomal reprogramming plasmids is likely to generate genetically stable iPSCs devoid of reprogramming factors, as seen in prior studies with EPCs<sup>103,104</sup> and episomal plasmids.<sup>51,52,105,106</sup> Third, the autofluorescence imaging technique is label-free, unlike other common methods to study metabolism such as electron microscopy, immunocytochemistry, and colorimetric metabolic assays. Autofluorescence imaging provides nondestructive real-time monitoring of live cells with lower sample phototoxicity compared with single-photon excitation.<sup>107</sup> Taken together, the processes of  $\mu$ CP platform fabrication, reprogramming, cell culture, autofluorescence imaging, iPSC identification based on machine learning models, and iPSC isolation can all be automated and extended to different reprogramming methods<sup>108</sup> (e.g., mRNA, Sendai virus), to other starting cell types (e.g., fibroblasts, keratinocytes), to other parameters (e.g., cell morphology,<sup>19–21</sup> mitochondrial structure<sup>71,76,109</sup>), and to other processes (e.g., differentiation<sup>110–113</sup>).

Limitations of our current approach include imaging resolution, culture duration, and per- $\mu$ Feature image analysis. First, comprehensive three-dimensional imaging of each  $\mu$ Feature could provide maps at higher resolution to further dissect the metabolic and nuclear changes occurring throughout the entire depth of the reprogramming cultures. Second, any discrepancy in the z-plane during OMI and confocal fluorescence image acquisition on the same sample could lead to discrepancies in the data that lead to poor classification of cell types by the random forest models. We mitigated this issue by programming a fixed z-plane for both OMI and confocal fluorescence image acquisition. Third, there is a limited duration of culture before cells overgrow within the  $\mu$ Feature. This could also result in cell detachment from the  $\mu$ Feature, which is difficult to image with OMI. For the reprogramming experiments described here, circular features with 300  $\mu$ m radius have been used for  $\sim$ 22 days of culture, although the cell seeding density or micropatterned geometry<sup>34,43,101</sup> could be easily changed. Fourth, because our primary focus was on identifying iPSCs that could be isolated to establish cell lines, this study did not distinguish the diverse cell states of IMs between day 8 and day 17 of reprogramming and subtle changes

in iPSC state. For instance, the intensity levels of NANOG and other key pluripotency transcription factors were not accounted for in our analyses, making it difficult to distinguish between partially reprogrammed cells, early and late stage iPSCs, and competing cells in culture.<sup>100,114–116</sup> Higher resolution staining for NANOG along with additional stem cell markers (e.g., TRA-1-60, MYC, OCT4, E-CADHERIN) could provide further insights into the differences between cell clusters identified in our analysis. Finally, imaging analysis was performed at different reprogramming time points on a per- $\mu$ Feature basis. Tracking single cells within the  $\mu$ Feature during reprogramming using cell tracking algorithms<sup>117</sup> could provide insights into metabolic and nuclear changes during reprogramming at a higher resolution.

Overall, we developed a high-throughput, noninvasive, rapid, and quantitative method to predict the reprogramming status of cells and study reprogramming heterogeneity. Our studies indicate that OMI can predict the reprogramming status of cells, which could enable real-time monitoring during iPSC manufacturing, thereby aiding in the identification of high-quality iPSCs in a timely and cost-effective manner. Similar technologies could impact other areas of cell manufacturing such as direct reprogramming, differentiation,<sup>110</sup> and cell line development.

### The Bigger Picture

Cell cultures undergoing epigenetic reprogramming are complex, as cells span a broad spectrum of cell states. In this study, we use two-photon microscopy to acquire high-dimensional data on the nuclear and metabolic characteristics of cells and develop machine learning models to predict reprogramming outcomes. This analysis can offer an orthogonal approach to investigating human somatic cell reprogramming that is complementary to the current studies of transcript and protein expression within reprogramming cells.

With further development, strategies using these imaging techniques could enable a rapid, automated, and standardized method to isolate iPSCs. This proof-of-principle study indicates that an image-based approach in conjunction with trajectory inference methods can elucidate cellular and subcellular changes that accompany human cell fate transitions.

## Materials and Methods

### EPC isolation and cell culture

EPCs were isolated from fresh peripheral human blood that was obtained from healthy donors (Interstate Blood Bank, Memphis, TN). Research using purchased de-identified blood specimens are not considered human subjects research under the US Common Rule. Blood was processed within 24 h of collection, where hematopoietic progenitor cells were extracted from whole blood using negative selection (RosetteSep; STEMCELL Technologies) and cultured in polystyrene tissue culture plates in erythroid expansion medium (STEMCELL Technologies) for 10 days to enrich for EPCs.

Enriched EPCs from day 10 were examined by staining with APC anti-human CD71 antibody (1:100; 334107; Biolegend) and incubating for 1 h at room temperature (RT). Data were collected on Attune NxT flow cytometer and analyzed with FlowJo.

### Micropattern design and polydimethylsiloxane stamp production

First, a template with the feature designs was created in AutoCAD (Autodesk). The template was then sent to the Advance Reproductions Corporation, MA, for the fabrication of a photomask, and a 6-inch (0.15 m) patterned silicon (Si) wafer was fabricated by the Microtechnology Core, University of Wisconsin-Madison, WI.<sup>118</sup> Using soft photolithography techniques, the Si wafer was spin coated with an SU-8 negative photoresist (MICRO CHEM) and exposed to UV light. The Si mold was then developed for 45 min in SU-8 developer (Sigma) that yielded features with a height of 150  $\mu\text{m}$ . The Si mold was then washed with acetone and isopropyl alcohol.

Elastomeric stamps used for microcontact printing were generated by standard soft lithographic techniques. The Si mold was rendered inert by overnight exposure in vapors of (tridecafluoro-1, 1, 2, 2-tetrahydrooctyl) trichlorosilane. Polydimethylsiloxane (PDMS; Sylgard 184 silicone elastomer base, 3097366-1004; Dow Corning) was prepared at a ratio of 1:10 curing agent (Sylgard 184 silicone elastomer curing agent, 3097358-1004; Dow Corning) and degassed in a vacuum for 30 min. The PDMS was then poured over the SU-8 Si mold on a hot plate and baked at 60°C overnight to create the PDMS stamp.

### $\mu\text{CP}$ well plate construction

$\mu\text{CP}$  substrates were constructed based on previous studies.<sup>47,48,119</sup> In brief, PDMS stamps with 300  $\mu\text{m}$  radius circular features were coated with Matrigel (WCell Research Institute) for 24 h. After 24 h, the Matrigel-coated PDMS stamp was dried with nitrogen and placed onto 35 mm cell culture-treated ibiTreat dishes (81156; Ibidi). A 50 g weight was added on top of the PDMS stamps to ensure even pattern transfer from the Matrigel-coated PDMS stamp to the ibiTreat dish.

This setup was incubated for 2 h at 37°C. The 35 mm ibiTreat dish was then backfilled with PLL (20 kDa)-*g*-(3.5)-PEG (2 kDa) (Susos), a graft polymer solution with a 20 kDa PLL backbone with 2 kDa PEG side chains, and a grafting ratio of 3.5 (mean PLL monomer units per PEG side chain), by using 0.1 mg/mL solution in 10 mM HEPES buffer for 30 min at RT. The ibiTreat dish was then washed with phosphate-buffered saline (PBS) and exposed to UV light for 15 min for sterilization to yield the micropatterned substrate.

### Reprogramming

On day 10, EPCs were electroporated with four episomal reprogramming plasmids encoding OCT4, shRNA knockdown of p53 (#27077; Addgene); SOX2, KLF4 (#27078; Addgene); L-MYC, LIN28 (#27080; Addgene); miR302-367 cluster (#98748; Addgene), using the P3 Primary Cell 4D-Nucleofector Kit (Lonza) and the EO-100 program.<sup>51,52</sup> Electroporated EPCs were seeded onto micropatterned substrates with erythroid expansion medium (STEMCELL Technologies) at a seeding density of 2000k cells per dish. Cells were supplemented with ReproTeSR (STEMCELL Technologies) on alternate days starting from day 3 without removing any medium from the well. On day 9, the medium was entirely switched to ReproTeSR, and the ReproTeSR medium was changed daily starting from day 10.

### Isolation of iPSCs

To isolate high-quality iPSC lines, candidate colonies were picked from micropatterns using a 200  $\mu\text{L}$  micropipette tip and transferred to Matrigel-coated polystyrene tissue culture plates in mTeSR1 medium (WCell Research Institute). If additional purification was required, one additional manual picking step with a 200  $\mu\text{L}$  micropipette tip was performed. During picking and subsequent passaging, the culture medium

was often supplemented with the Rho kinase inhibitor Y-27632 (Sigma-Aldrich) at a 10  $\mu\text{M}$  concentration to encourage cell survival and establish clonal lines. iPSCs obtained from EPCs were maintained in mTeSR1 medium on Matrigel-coated polystyrene tissue culture plates and passaged with ReLeSR (STEMCELL Technologies) every 3–5 days. All cells were maintained at 37°C and 5%  $\text{CO}_2$ .

### Antibodies and staining

All cells were fixed for 15 min with 4% paraformaldehyde in PBS (Sigma-Aldrich) and permeabilized with 0.5% Triton-X (Sigma-Aldrich) for >4 h at RT before staining. Hoechst (H1399; Thermo Fisher Scientific, Waltham, MA) was used at 5  $\mu\text{g}/\text{mL}$  with 15 min incubation at RT to stain nuclei. Primary antibodies were applied overnight at 4°C in a blocking buffer of 5% donkey serum (Sigma-Aldrich) at the following concentrations: anti-laminin (L9393; Sigma-Aldrich) 1:500; TRA-1-60 (MAB4360; EMD Millipore, Burlington, MA) 1:100; NANOG (AF1997; R&D Systems) 1:200; CD71 (334107; Biolegend) 1:100.

Secondary antibodies were obtained from Thermo Fisher Scientific and applied in a blocking buffer of 5% donkey serum for 1 h at RT at concentrations of 1:400 to 1:800. A Nikon Eclipse Ti epifluorescence microscope was used to acquire single 10 $\times$  images of each micropattern, and a Nikon AR1 confocal microscope was used to acquire 60 $\times$  stitched images of each micropattern using the z-plane closest to the micropatterned substrate for reprogramming studies. In brief, EPCs are identified as CD71<sup>+</sup>; Nanog<sup>-</sup>, IMs are indicated as CD71<sup>-</sup>; Nanog<sup>-</sup>, and iPSCs are indicated as CD71<sup>-</sup>; Nanog<sup>+</sup>.

### Autofluorescence imaging of NAD(P)H and FAD

Fluorescence lifetime imaging was performed at different time points during reprogramming by an Ultima two-photon microscope (Bruker) composed of an ultrafast tunable excitation laser source (Insight DS+; Spectra-Physics) coupled to a Nikon Ti-E inverted microscope with time-correlated single-photon counting electronics (SPC-150; Becker & Hickl). The laser source enables sequential excitation of NAD(P)H at 750 nm and FAD at 890 nm. NAD(P)H and FAD images were acquired through 440/80 and 550/100 nm bandpass filters (Chroma), respectively, using gallium arsenide phosphide photomultiplier tubes (H7422; Hamamatsu).

The laser power at the sample was  $\sim 3.5$  mW for NAD(P)H and 6 mW for FAD. Lifetime imaging using time-correlated single-photon counting electronics (SPC-150; Becker & Hickl) was performed within Prairie View Atlas Mosaic Imaging (Bruker Fluorescence Microscopy) to capture the entire  $\mu\text{Feature}$ . Fluorescence lifetime decays with 512-time bins were acquired across 512 $\times$ 512-pixel images with a pixel dwell time of 4.8  $\mu\text{s}$  and an integration period of 60 s. Photon count rates were  $\sim 1\text{--}5 \times 10^5$  and monitored during image acquisition to ensure that no photobleaching occurred.

All samples were placed on a stage-op incubator and illuminated through a 40 $\times$ /1.15 NA objective (Nikon). The short lifetime of red blood cell fluorescence at 890 nm was used as the instrument response function and had a full-width half maximum of 240 ps. A yellow green (YG) fluorescent bead (YG microspheres, Polysciences Inc.;  $\tau = 2.13 \pm 0.03$  ns,  $n = 6$ ) was imaged daily as a fluorescence lifetime standard.<sup>35,120</sup>

### Image analysis

Fluorescence lifetime decays were analyzed to extract fluorescence lifetime components through SPCImage software (Becker & Hickl). A threshold was used to exclude pixels with low fluorescence signals (i.e., background). A bin of 3 $\times$ 3 pixels was used to maintain spatial

resolution, the fluorescence lifetime decay curve was convolved with the instrument response function and fit to a two-component exponential decay model,  $I(t) = \alpha_1 e^{-t/\tau_1} + \alpha_2 e^{-t/\tau_2} + C$ , where  $I(t)$  is the fluorescence intensity as a function of time  $t$  after the laser pulse,  $\alpha_1$  and  $\alpha_2$  are the fractional contributions of the short and long lifetime components, respectively (i.e.,  $\alpha_1 + \alpha_2 = 1$ ),  $\tau_1$  and  $\tau_2$  are the short and long lifetime components, respectively, and  $C$  accounts for background light.

Both NAD(P)H and FAD can exist in quenched (short lifetime) and unquenched (long lifetime) configurations<sup>39,40</sup>; the fluorescence decays of NAD(P)H and FAD are, therefore, fit to two components. Fluorescence intensity images were generated by integrating photon counts over the per-pixel fluorescence decays.

Images were analyzed at the single-cell level to evaluate cellular heterogeneity.<sup>121</sup>

A pixel classifier was trained on 15 images using *ilastik*<sup>60</sup> software to identify the pixels within the nuclei in NAD(P)H images. An object classifier was then used to identify the nuclei in NAD(P)H images using the pixel classifier along with the following parameters: Method=Simple, Threshold=0.3, Smooth=1, Size Filter Min=15 pixels, Size Filter Max=500 pixels. A customized *CellProfiler*<sup>61</sup> pipeline was then used to obtain metabolic and nuclear parameters. The *CellProfiler* pipeline applied the following steps: Primary objects (nuclei) were inputted from *ilastik*. Secondary objects (cells) were then identified in the NAD(P)H intensity image by outward propagation of the primary objects.

Cytoplasm masks were determined by subtracting the nucleus mask from the cell mask. Cytoplasm masks were applied to all images to determine single-cell redox ratio and NAD(P)H and FAD lifetime parameters. A total of 11 metabolic parameters were analyzed for each cell cytoplasm (Supplementary Fig. S1D): NAD(P)H intensity ( $I_{\text{NAD(P)H}}$ ), NAD(P)H  $\alpha_1$ , NAD(P)H  $\tau_1$ , NAD(P)H  $\tau_2$ , NAD(P)H mean lifetime ( $\tau_m = \alpha_1 \tau_1 + \alpha_2 \tau_2$ ), FAD intensity ( $I_{\text{FAD}}$ ), FAD  $\alpha_1$ , FAD  $\tau_1$ , FAD  $\tau_2$ , FAD  $\tau_m$ , optical redox ratio [ $I_{\text{NAD(P)H}} / (I_{\text{NAD(P)H}} + I_{\text{FAD}})$ ]. A total of eight nuclear parameters were analyzed for each nucleus: area, perimeter, MeanRad, NSI, solidity, extent, number of neighbors (#Neigh), and distance to closest neighbor (1stNeigh).

Representative images of the optical redox ratio, NAD(P)H  $\tau_m$  and FAD  $\tau_m$ , were computed using the *Fiji* software.

## UMAP clustering

Clustering of cells across EPCs, IMs, and iPSCs was represented using UMAP. UMAP dimensionality reduction<sup>66</sup> was implemented using R on all 11 OMI parameters (optical redox ratio, NAD(P)H  $\tau_m$ ,  $\tau_1$ ,  $\tau_2$ ,  $\alpha_1$ ,  $\alpha_2$ ; FAD  $\tau_m$ ,  $\tau_1$ ,  $\tau_2$ ,  $\alpha_1$ ,  $\alpha_2$ ) and/or all 8 nuclear parameters (area, perimeter, MeanRad, NSI, solidity, extent, #Neigh, 1stNeigh) for projection in two-dimensional space. The following parameters were used for UMAP visualizations: "n\_neighbors": 20; "min\_dist": 0.3, "metric": Jaccard, "n\_components": 2.

## z-Score hierarchical clustering

z-Score of each metabolic and nuclear parameter for each cell was calculated.  $z\text{-Score} = (\mu_{\text{observed}} - \mu_{\text{row}}) / \sigma_{\text{row}}$ , where  $\mu_{\text{observed}}$  is the mean value of each parameter for each cell;  $\mu_{\text{row}}$  is the mean value of each parameter for all cells together, and  $\sigma_{\text{row}}$  is the standard deviation of each parameter across all cells. Heatmaps of z-scores for all OMI variables were generated to visualize differences in each parameter between different cells. Dendrograms show clustering based on the similarity of average Euclidean distances across all variable z-scores. Heatmaps and associated dendrograms were generated in Python.

## Classification methods

Random forest, simple logistic, k-nearest neighbor (IBk), and naive Bayes classification methods were trained to classify reprogramming cells into EPCs, IMs, and iPSCs using Weka software.<sup>122</sup> All data were randomly partitioned into training and test data sets using 15-fold cross-validation for training and test proportions of 93.3% (1994 cells) and 6.7% (143 cells), respectively. Cross-validation of EPCs, IMs, and iPSCs was performed using immunostaining data. Each model was replicated 100 times; new training and test data were generated before each iteration.

Parameter weights for metabolic and nuclear parameters were extracted using the *GainRatioAttributeEval* function in Weka to determine the contribution of each variable to the trained classification models. One-vs-rest ROC curves were generated to evaluate the classification model performance on the classification of test set data and are the average of 100 iterations of data that was randomly selected from training and test sets. All the ROC curves displayed were constructed from the test data sets using the model generated from the training data sets.

## Karyotyping

Cells cultured for at least five passages were grown to 60–80% confluence and shipped for karyotype analysis to WiCell Research Institute, Madison, WI. G-banded karyotyping was performed using standard cytogenetic protocols.<sup>123</sup> Metaphase preparations were digitally captured with Applied Spectral Imaging software and hardware. For each cell line, 20 GTL-banded metaphases were counted, of which a minimum of 5 was analyzed and karyotyped. Results were reported in accordance with guidelines established by the International System for Cytogenetic Nomenclature 2016.<sup>124</sup>

## Statistics

*p*-Values were calculated using the nonparametric Kruskal–Wallis test for multiple unmatched comparisons with GraphPad Prism software. Statistical tests were deemed significant at  $\alpha \leq 0.05$ . Technical replicates are defined as distinct  $\mu$ Features within an experiment. Biological replicates are experiments performed with different donors. No *a priori* power calculations were performed.

## Pseudotime trajectories

To order cells by pseudotime, EPCs were designated the starting point. We used *Monocle3* to define a pseudo-reprogramming time trajectory, termed pseudotime, where cells are linearly ordered relative to their progress or change in metabolic and nuclear parameters relative to the starting EPC population. The lengths of the trajectory between each branch point were used to define state by the *Monocle3* algorithm implemented in Rstudio Version 1.3.1073 as described in CodeS1.R file.

## Authors' Contributions

Conceptualization of the study occurred by K.M. and K.S. Experimental design was carried out by K.M., T.M.H., M.C.S., and K.S. Methodology was done by K.M., T.M.H., and J.R. Data analysis was carried out by K.M., G.A.B., and E.C.G. Supervision was carried out by K.S. and M.C.S. Writing—original draft—was by K.M. Writing—review and editing—was by K.M., K.S., and M.C.S.

## Acknowledgments

We thank members of the Saha laboratory for helpful discussion and comments on the article. Furthermore, we thank members of the Skala laboratory for discussions about machine learning

classification methods. We also thank plasmid depositors to Addgene, and James Thomson's laboratory for sharing the miR302-367 plasmid. We thank the Interstate Blood Bank for supplying fresh blood, Jose Jimenez for manufacturing the silicon mold, and Brett Napiwocki for help with PDMS stamp preparation. We thank Matthew Stefely for the assistance with figure illustrations.

### Data and Materials Availability

All data needed to evaluate conclusions in the article are included in the article and/or Supplementary Materials. Additional data related to this article may be requested from the authors.

### Author Disclosure Statement

K.M., K.S., and M.C.S. have filed a patent application on this study. The remaining authors declare no competing financial interests.

### Funding Information

This study was funded by National Science Foundation (CBET-1350178); National Institutes of Health (R35 GM119644, U01 EY032333, R01 CA211082, R01 CA205101, R01 CA185747); University of Wisconsin-Madison Stem Cell and Regenerative Medicine Center; Wisconsin Institute for Discovery; Wisconsin Alumni Research Foundation; Morgridge Institute for Research; Retina Research Foundation Kathryn and Latimer Murfee Chair, McPherson ERI; and Retina Research Foundation Daniel M. Albert Chair, McPherson ERI.

### Supplementary Material

Supplementary Data

### References

- Saha K, Jaenisch R. Technical challenges in using human induced pluripotent stem cells to model disease. *Cell Stem Cell*. 2009;5:584–595. DOI: 10.1016/j.stem.2009.11.009.
- Laustriat D, Gide J, Peschanski M. Human pluripotent stem cells in drug discovery and predictive toxicology. *Biochem Soc Trans*. 2010;38:1051–1057. DOI: 10.1042/BST0381051.
- Ferreira LMR, Mostajo-Radji MA. How induced pluripotent stem cells are redefining personalized medicine. *Gene*. 2013;520:1–6. DOI: 10.1016/j.gene.2013.02.037.
- Schweitzer JS, Song B, Herrington TM, et al. Personalized iPSC-derived dopamine progenitor cells for Parkinson's disease. *N Engl J Med*. 2020;382:1926–1932. DOI: 10.1056/NEJMoa1915872.
- Takagi S, Mandai M, Gocho K, et al. Evaluation of transplanted autologous induced pluripotent stem cell-derived retinal pigment epithelium in exudative age-related macular degeneration. *Ophthalmol Retina*. 2019;3:850–859. DOI: 10.1016/j.oret.2019.04.021.
- Mandai M, Watanabe A, Kurimoto Y, et al. Autologous induced stem-cell-derived retinal cells for macular degeneration. *N Engl J Med*. 2017;376:1038–1046. DOI: 10.1056/NEJMoa1608368.
- Yamanaka S. Pluripotent stem cell-based cell therapy—promise and challenges. *Cell Stem Cell*. 2020;27:523–531. DOI: 10.1016/j.stem.2020.09.014.
- Madrid M, Sumen C, Aivio S, et al. Autologous induced pluripotent stem cell-based cell therapies: promise, progress, and challenges. *Curr Protoc*. 2021;1; DOI: 10.1002/cpz1.88.
- Silva M, Daheron L, Hurley H, et al. Generating iPSCs: translating cell reprogramming science into scalable and robust biomanufacturing strategies. *Cell Stem Cell*. 2015;16:13–17. DOI: 10.1016/j.stem.2014.12.013.
- Yaffe MP, Noggle SA, Solomon SL. Raising the standards of stem cell line quality. *Nat Cell Biol*. 2016;18:236–237. DOI: 10.1038/ncb3313.
- Huang C-Y, Liu C-L, Ting C-Y, et al. Human iPSC banking: barriers and opportunities. *J Biomed Sci*. 2019;26:87. DOI: 10.1186/s12929-019-0578-x.
- Jo H-Y, Han H-W, Jung I, et al. Development of genetic quality tests for good manufacturing practice-compliant induced pluripotent stem cells and their derivatives. *Sci Rep*. 2020;10:3939. DOI: 10.1038/s41598-020-60466-9.
- Sullivan S, Stacey GN, Akazawa C, et al. Quality control guidelines for clinical-grade human induced pluripotent stem cell lines. *Regen Med*. 2018;13:859–866. DOI: 10.2217/rme-2018-0095.
- Ounkomol C, Seshamani S, Maleckar MM, et al. Label-free prediction of three-dimensional fluorescence images from transmitted-light microscopy. *Nat Methods*. 2018;15:917–920. DOI: 10.1038/s41592-018-0111-2.
- Kandel ME, He YR, Lee YJ, et al. Phase imaging with computational specificity (PICS) for measuring dry mass changes in sub-cellular compartments. *Nat Commun*. 2020;11:6256. DOI: 10.1038/s41467-020-20062-x.
- Nguyen TC, Bui V, Thai A, et al. Virtual organelle self-coding for fluorescence imaging via adversarial learning. *J Biomed Opt*. 2020;25; DOI: 10.1117/1.JBO.25.9.096009.
- Wieslander H, Gupta A, Bergman E, et al. Learning to see colours: generating biologically relevant fluorescent labels from bright-field images. *Bioinformatics*. 2021. DOI: 10.1101/2021.01.18.427121.
- Christiansen EM, Yang SJ, Ando DM, et al. In silico labeling: predicting fluorescent labels in unlabeled images. *Cell*. 2018;173:792–803.e19. DOI: 10.1016/j.cell.2018.03.040.
- Chan EM, Ratanasirintrao S, Park I-H, et al. Live cell imaging distinguishes bona fide human IPS cells from partially reprogrammed cells. *Nat Biotechnol*. 2009;27:1033–1037. DOI: 10.1038/nbt.1580.
- Tokunaga K, Saitoh N, Goldberg IG, et al. Computational image analysis of colony and nuclear morphology to evaluate human induced pluripotent stem cells. *Sci Rep*. 2015;4:6996. DOI: 10.1038/srep06996.
- Kato R, Matsumoto M, Sasaki H, et al. Parametric analysis of colony morphology of non-labelled live human pluripotent stem cells for cell quality control. *Sci Rep*. 2016;6:34009. DOI: 10.1038/srep34009.
- Fischbacher B, Hedaya S, Hartley BJ, et al. Modular deep learning enables automated identification of monoclonal cell lines. *Nat Mach Intell*. 2021;3:632–640. DOI: 10.1038/s42256-021-00354-7.
- Vander Heiden MG, Cantley LC, Thompson CB. Understanding the Warburg effect: the metabolic requirements of cell proliferation. *Science*. 2009;324:1029–1033. DOI: 10.1126/science.1160809.
- Panopoulos AD, Yanes O, Ruiz S, et al. The metabolome of induced pluripotent stem cells reveals metabolic changes occurring in somatic cell reprogramming. *Cell Res*. 2012;22:168–177. DOI: 10.1038/cr.2011.177.
- Nishimura K, Fukuda A, Hisatake K. Mechanisms of the metabolic shift during somatic cell reprogramming. *Int J Mol Sci*. 2019;20:2254. DOI: 10.3390/ijms20092254.
- Mathieu J, Ruohola-Baker H. Metabolic remodeling during the loss and acquisition of pluripotency. *Development*. 2017;144:541–551. DOI: 10.1242/dev.128389.
- Rigaud VOC, Hoy R, Mohsin S, et al. Stem cell metabolism: powering cell-based therapeutics. *Cells*. 2020;9:2490. DOI: 10.3390/cells9112490.
- Kida YS, Kawamura T, Wei Z, et al. ERRs mediate a metabolic switch required for somatic cell reprogramming to pluripotency. *Cell Stem Cell*. 2015;16:547–555. DOI: 10.1016/j.stem.2015.03.001.
- Ishida T, Nakao S, Ueyama T, et al. Metabolic remodeling during somatic cell reprogramming to induced pluripotent stem cells: involvement of hypoxia-inducible factor 1. *Inflamm Regen*. 2020;40:8. DOI: 10.1186/s41232-020-00117-8.
- Zhu S, Li W, Zhou H, et al. Reprogramming of human primary somatic cells by OCT4 and chemical compounds. *Cell Stem Cell*. 2010;7:651–655. DOI: 10.1016/j.stem.2010.11.015.
- Yoshida Y, Takahashi K, Okita K, et al. Hypoxia enhances the generation of induced pluripotent stem cells. *Cell Stem Cell*. 2009;5:237–241. DOI: 10.1016/j.stem.2009.08.001.
- Cordie T, Harkness T, Jing X, et al. Nanofibrous electrospun polymers for reprogramming human cells. *Cell Mol Bieng*. 2014;7:379–393. DOI: 10.1007/s12195-014-0341-z.
- Mattout A, Biran A, Meshorer E. Global epigenetic changes during somatic cell reprogramming to IPS cells. *J Mol Cell Biol*. 2011;3:341–350. DOI: 10.1093/jmcb/mjr028.
- Molugu K, Harkness T, Carlson-Stevermer J, et al. Tracking and predicting human somatic cell reprogramming using nuclear characteristics. *Biophys J*. 2020;118:2086–2102. DOI: 10.1016/j.bpj.2019.10.014.

35. Skala MC, Ricking KM, Gendron-Fitzpatrick A, et al. In vivo multiphoton microscopy of NADH and FAD redox states, fluorescence lifetimes, and cellular morphology in precancerous epithelia. *Proc Natl Acad Sci U S A*. 2007;104:19494–19499. DOI: 10.1073/pnas.0708425104.
36. Huang S, Heikal AA, Webb WW. Two-photon fluorescence spectroscopy and microscopy of NAD(P)H and flavoprotein. *Biophys J*. 2002;82:2811–2825. DOI: 10.1016/S0006-3495(02)75621-X.
37. Chance B, Schoener B, Oshino R, et al. Oxidation-reduction ratio studies of mitochondria in freeze-trapped samples. NADH and flavoprotein fluorescence signals. *J Biol Chem*. 1979;254:4764–4771. DOI: 10.1016/S0021-9258(17)30079-0.
38. Georgakoudi I, Quinn KP. Optical imaging using endogenous contrast to assess metabolic state. *Annu Rev Biomed Eng*. 2012;14:351–367. DOI: 10.1146/annurev-bioeng-071811-150108.
39. Nakashima N, Yoshihara K, Tanaka F, et al. Picosecond fluorescence lifetime of the coenzyme of D-amino acid oxidase. *J Biol Chem*. 1980;255:5261–5263. DOI: 10.1016/S0021-9258(19)70779-0.
40. Lakowicz JR. Fluorescence lifetime imaging of free and protein-bound NADH. *Proc Natl Acad Sci U S A*. 1992;89:1271–1275.
41. Datta R, Heaster TM, Sharick JT, et al. Fluorescence lifetime imaging microscopy: fundamentals and advances in instrumentation, analysis, and applications. *J Biomed Opt*. 2020;25:1. DOI: 10.1117/1.JBO.25.7.071203.
42. Pouli D, Thieu H-T, Genega EM, et al. Label-free, high-resolution optical metabolic imaging of human cervical precancers reveals potential for intraepithelial neoplasia diagnosis. *Cell Rep Med*. 2020;1:100017. DOI: 10.1016/j.xcrm.2020.100017.
43. Harkness T, McNulty JD, Prestil R, et al. High-content imaging with micro-patterned multiwell plates reveals influence of cell geometry and cytoskeleton on chromatin dynamics. *Biotechnol J*. 2015;10:1555–1567. DOI: 10.1002/biot.201400756.
44. Fink J, Théry M, Azioune A, et al. Comparative study and improvement of current cell micro-patterning techniques. *Lab Chip*. 2007;7:672–680. DOI: 10.1039/B618545B.
45. Trapnell C, Cacchiarelli D, Grimsby J, et al. The dynamics and regulators of cell fate decisions are revealed by pseudotemporal ordering of single cells. *Nat Biotechnol*. 2014;32:381–386. DOI: 10.1038/nbt.2859.
46. Carlson-Stevermer J, Goedland M, Steyer B, et al. High-content analysis of CRISPR-Cas9 gene-edited human embryonic stem cells. *Stem Cell Reports*. 2016;6:109–120. DOI: 10.1016/j.stemcr.2015.11.014.
47. Liazoghli D, Roth AD, Thostrup P, et al. Substrate micropatterning as a new in vitro cell culture system to study myelination. *ACS Chem Neurosci*. 2012;3:90–95. DOI: 10.1021/cn2000734.
48. Csucs G, Michel R, Lussi JW, et al. Microcontact printing of novel co-polymers in combination with proteins for cell-biological applications. *Biomaterials*. 2003;24:1713–1720. DOI: 10.1016/S0142-9612(02)00568-9.
49. Hughes CS, Postovit LM, Lajoie GA. Matrigel: a complex protein mixture required for optimal growth of cell culture. *Proteomics*. 2010;10:1886–1890. DOI: 10.1002/pmic.200900758.
50. Dong HY, Wilkes S, Yang H. CD71 is selectively and ubiquitously expressed at high levels in erythroid precursors of all maturation stages: a comparative immunochemical study with glycophorin A and hemoglobin A. *Am J Surg Pathol*. 2011;35:10.
51. Okita K, Yamakawa T, Matsumura Y, et al. An efficient nonviral method to generate integration-free human-induced pluripotent stem cells from cord blood and peripheral blood cells. *Stem Cells*. 2013;31:458–466. DOI: 10.1002/stem.1293.
52. Howden SE, Maufort JP, Duffin BM, et al. Simultaneous reprogramming and gene correction of patient fibroblasts. *Stem Cell Reports*. 2015;5:1109–1118. DOI: 10.1016/j.stemcr.2015.10.009.
53. Polo JM, Anderssen E, Walsh RM, et al. A molecular roadmap of reprogramming somatic cells into IPS cells. *Cell*. 2012;151:1617–1632. DOI: 10.1016/j.cell.2012.11.039.
54. Zhang J, Nuebel E, Daley GQ, et al. Metabolic regulation in pluripotent stem cells during reprogramming and self-renewal. *Cell Stem Cell*. 2012;11:589–595. DOI: 10.1016/j.stem.2012.10.005.
55. Zhang J, Zhao J, Dahan P, et al. Metabolism in pluripotent stem cells and early mammalian development. *Cell Metab*. 2018;27:332–338. DOI: 10.1016/j.cmet.2018.01.008.
56. Ryall JG, Cliff T, Dalton S, et al. Metabolic reprogramming of stem cell epigenetics. *Cell Stem Cell*. 2015;17:651–662. DOI: 10.1016/j.stem.2015.11.012.
57. Sun H, Yang X, Liang L, et al. Metabolic switch and epithelial–mesenchymal transition cooperate to regulate pluripotency. *EMBO J*. 2020;39. DOI: 10.15252/embj.2019102961.
58. Xu X, Duan S, Yi F, et al. Mitochondrial regulation in pluripotent stem cells. *Cell Metab*. 2013;18:325–332. DOI: 10.1016/j.cmet.2013.06.005.
59. Kolenc OI, Quinn KP. Evaluating cell metabolism through autofluorescence imaging of NAD(P)H and FAD. *Antioxid Redox Signal*. 2019;30:875–889. DOI: 10.1089/ars.2017.7451.
60. Berg S, Kutra D, Kroeger T, et al. Ilastik: interactive machine learning for (Bio)Image analysis. *Nat Methods*. 2019;16:1226–1232. DOI: 10.1038/s41592-019-0582-9.
61. Carpenter AE, Jones TR, Lamprecht MR, et al. CellProfiler: image analysis software for identifying and quantifying cell phenotypes. *Genome Biol*. 2006;7:R100. DOI: 10.1186/gb-2006-7-10-r100.
62. Sullivan WJ, Mullen PJ, Schmid EW, et al. Extracellular matrix remodeling regulates glucose metabolism through TXNIP destabilization. *Cell*. 2018;175:117–132.e21. DOI: 10.1016/j.cell.2018.08.017.
63. Hu H, Juvekar A, Lyssiotis CA, et al. Phosphoinositide 3-kinase regulates glycolysis through mobilization of aldolase from the actin cytoskeleton. *Cell*. 2016;164:433–446. DOI: 10.1016/j.cell.2015.12.042.
64. Bays JL, Campbell HK, Heidema C, et al. Linking E-cadherin mechanotransduction to cell metabolism through force-mediated activation of AMPK. *Nat Cell Biol*. 2017;19:724–731. DOI: 10.1038/ncb3537.
65. Park JS, Burckhardt CJ, Lazcano R, et al. Mechanical regulation of glycolysis via cytoskeleton architecture. *Nature*. 2020;578:621–626. DOI: 10.1038/s41586-020-1998-1.
66. McInnes L, Healy J, Saul N, et al. UMAP: Uniform manifold approximation and projection. *J Open Source Software*. 2018;3:861. DOI: 10.21105/joss.00861.
67. Amancio DR, Comin CH, Casanova D, et al. A systematic comparison of supervised classifiers. *PLoS One*. 2014;9:e94137. DOI: 10.1371/journal.pone.0094137.
68. Bendall SC, Davis KL, Amir ED, et al. Single-cell trajectory detection uncovers progression and regulatory coordination in human B cell development. *Cell*. 2014;157:714–725. DOI: 10.1016/j.cell.2014.04.005.
69. Qiu X, Mao Q, Tang Y, et al. Reversed graph embedding resolves complex single-cell trajectories. *Nat Methods*. 2017;14:979–982. DOI: 10.1038/nmeth.4402.
70. Moran PAP. Notes on continuous stochastic phenomena. *Biometrika*. 1950;37:17–23. DOI: 10.2307/2332142.
71. Prigione A, Fauler B, Lurz R, et al. The senescence-related mitochondrial/oxidative stress pathway is repressed in human induced pluripotent stem cells. *Stem Cells*. 2010;28:721–733. DOI: 10.1002/stem.404.
72. Prieto J, León M, Ponsoda X, et al. Early ERK1/2 activation promotes DRP1-dependent mitochondrial fission necessary for cell reprogramming. *Nat Commun*. 2016;7:11124. DOI: 10.1038/ncomms11124.
73. Hawkins KE, Joy S, Delhove JMKM, et al. NRF2 orchestrates the metabolic shift during induced pluripotent stem cell reprogramming. *Cell Rep*. 2016;14:1883–1891. DOI: 10.1016/j.celrep.2016.02.003.
74. Cacchiarelli D, Trapnell C, Ziller MJ, et al. Integrative analyses of human reprogramming reveal dynamic nature of induced pluripotency. *Cell*. 2015;162:412–424. DOI: 10.1016/j.cell.2015.06.016.
75. Mathieu J, Zhou W, Xing Y, et al. Hypoxia-inducible factors have distinct and stage-specific roles during reprogramming of human cells to pluripotency. *Cell Stem Cell*. 2014;14:592–605. DOI: 10.1016/j.stem.2014.02.012.
76. Folmes CDL, Nelson TJ, Martinez-Fernandez A, et al. Somatic oxidative bioenergetics transitions into pluripotency-dependent glycolysis to facilitate nuclear reprogramming. *Cell Metab*. 2011;14:264–271. DOI: 10.1016/j.cmet.2011.06.011.
77. Reid MA, Dai Z, Locasale JW. The impact of cellular metabolism on chromatin dynamics and epigenetics. *Nat Cell Biol*. 2017;19:1298–1306. DOI: 10.1038/ncb3629.
78. Mattout A, Cabianga DS, Gasser SM. Chromatin states and nuclear organization in development—a view from the nuclear lamina. *Genome Biol*. 2015;16:174. DOI: 10.1186/s13059-015-0747-5.
79. Stephens AD, Liu PZ, Banigan EJ, et al. Chromatin histone modifications and rigidity affect nuclear morphology independent of lamins. *Mol Biol Cell*. 2018;29:220–233. DOI: 10.1091/mbc.E17-06-0410.
80. Orkin SH, Hochedlinger K. Chromatin connections to pluripotency and cellular reprogramming. *Cell*. 2011;145:835–850. DOI: 10.1016/j.cell.2011.05.019.
81. Apostolou E, Hochedlinger K. Chromatin dynamics during cellular reprogramming. *Nature*. 2013;502:462–471. DOI: 10.1038/nature12749.

82. Liu Z, Pouli D, Alonzo CA, et al. Mapping metabolic changes by noninvasive, multiparametric, high-resolution imaging using endogenous contrast. *Sci Adv.* 2018;4:eaap9302. DOI: 10.1126/sciadv.aap9302.
83. Sato K, Nishina Y, Shiga K, et al. Hydrogen-bonding dynamics of free flavins in benzene and FAD in electron-transferring flavoprotein upon excitation. *J Photochem Photobiol B.* 2003;70:67–73. DOI: 10.1016/S1011-1344(03)00056-3.
84. Mueller F, Mayhew SG, Massey V. Effect of temperature on the absorption spectra of free and protein-bound flavines. *Biochemistry.* 1973;12:4654–4662. DOI: 10.1021/bi00747a017.
85. Schneckenburger H, Wagner M, Weber P, et al. Autofluorescence lifetime imaging of cultivated cells using a UV picosecond laser diode. *J Fluoresc.* 2004;14:649–654. DOI: 10.1023/B:JOFI.0000039351.09916.cc.
86. Zbinden A, Carvajal Berrio DA, Urbanczyk M, et al. Fluorescence lifetime metabolic mapping of hypoxia-induced damage in pancreatic pseudocysts. *J Biophotonics.* 2020;13. DOI: 10.1002/jbio.202000375.
87. Soufi A, Donahue G, Zaret KS. Facilitators and impediments of the pluripotency reprogramming factors' initial engagement with the genome. *Cell.* 2012;151:994–1004. DOI: 10.1016/j.cell.2012.09.045.
88. Li R, Liang J, Ni S, et al. A mesenchymal-to-epithelial transition initiates and is required for the nuclear reprogramming of mouse fibroblasts. *Cell Stem Cell.* 2010;7:51–63. DOI: 10.1016/j.stem.2010.04.014.
89. Mikkelsen TS, Hanna J, Zhang X, et al. Dissecting direct reprogramming through integrative genomic analysis. *Nature.* 2008;454:49–55. DOI: 10.1038/nature07056.
90. Samavarchi-Tehrani P, Golipour A, David L, et al. Functional genomics reveals a BMP-driven mesenchymal-to-epithelial transition in the initiation of somatic cell reprogramming. *Cell Stem Cell.* 2010;7:64–77. DOI: 10.1016/j.stem.2010.04.015.
91. Buganim Y, Faddah DA, Cheng AW, et al. Single-cell expression analyses during cellular reprogramming reveal an early stochastic and a late hierarchic phase. *Cell.* 2012;150:1209–1222. DOI: 10.1016/j.cell.2012.08.023.
92. Zunder ER, Lujan E, Goltsev Y, et al. A continuous molecular roadmap to iPSC reprogramming through progression analysis of single-cell mass cytometry. *Cell Stem Cell.* 2015;16:323–337. DOI: 10.1016/j.stem.2015.01.015.
93. Kim DH, Marinov GK, Pepke S, et al. Single-cell transcriptome analysis reveals dynamic changes in lncRNA expression during reprogramming. *Cell Stem Cell.* 2015;16:88–101. DOI: 10.1016/j.stem.2014.11.005.
94. Lujan E, Zunder ER, Ng YH, et al. Early reprogramming regulators identified by prospective isolation and mass cytometry. *Nature.* 2015;521:352–356. DOI: 10.1038/nature14274.
95. Nguyen QH, Lukowski SW, Chiu HS, et al. Single-cell RNA-Seq of human induced pluripotent stem cells reveals cellular heterogeneity and cell state transitions between subpopulations. *Genome Res.* 2018;28:1053–1066. DOI: 10.1101/gr.223925.117.
96. Schiebinger G, Shu J, Tabaka M, et al. Optimal-transport analysis of single-cell gene expression identifies developmental trajectories in reprogramming. *Cell.* 2019;176:928–943.e22. DOI: 10.1016/j.cell.2019.01.006.
97. Bidy BA, Kong W, Kamimoto K, et al. Single-cell mapping of lineage and identity in direct reprogramming. *Nature.* 2018;564:219–224. DOI: 10.1038/s41586-018-0744-4.
98. Tran KA, Pietrzak SJ, Zaidan NZ, et al. Defining reprogramming checkpoints from single-cell analyses of induced pluripotency. *Cell Rep.* 2019;27:1726–1741.e5. DOI: 10.1016/j.celrep.2019.04.056.
99. Zhao T, Fu Y, Zhu J, et al. Single-Cell RNA-Seq reveals dynamic early embryonic-like programs during chemical reprogramming. *Cell Stem Cell.* 2018;23:31–45.e7. DOI: 10.1016/j.stem.2018.05.025.
100. Rui Q, Song Y, Delon C-X. Diversification of reprogramming trajectories revealed by parallel single-cell transcriptome and chromatin accessibility sequencing. *Sci Adv.* 2020;19.
101. McNulty JD, Klann T, Sha J, et al. High-precision robotic microcontact printing (R-MCP) utilizing a vision guided selectively compliant articulated robotic arm. *Lab Chip.* 2014;14:1923–1930. DOI: 10.1039/C3LC51137E.
102. D'Arcangelo E, McGuigan AP. Micropatterning strategies to engineer controlled cell and tissue architecture in vitro. *BioTechniques.* 2015;58. DOI: 10.2144/000114245.
103. Chou B-K, Mali P, Huang X, et al. Efficient human IPS cell derivation by a non-integrating plasmid from blood cells with unique epigenetic and gene expression signatures. *Cell Res.* 2011;21:518–529. DOI: 10.1038/cr.2011.12.
104. Mack AA, Kroboth S, Rajesh D, et al. Generation of induced pluripotent stem cells from CD34+ cells across blood drawn from multiple donors with non-integrating episomal vectors. *PLoS One.* 2011;6:e27956. DOI: 10.1371/journal.pone.0027956.
105. Nanbo A, Sugden A, Sugden B. The coupling of synthesis and partitioning of EBV's plasmid replicon is revealed in live cells. *EMBO J.* 2007;26:4252–4262. DOI: 10.1038/sj.emboj.7601853.
106. Yu J, Hu K, Smuga-Otto K, et al. Human induced pluripotent stem cells free of vector and transgene sequences. *Science.* 2009;324:797–801. DOI: 10.1126/science.1172482.
107. Squirrel JM, Wokosin DL, White JG, et al. Long-term two-photon fluorescence imaging of mammalian embryos without compromising viability. *Nat Biotechnol.* 1999;17:763–767. DOI: 10.1038/11698.
108. Schlaeger TM, Daheron L, Brickler TR, et al. A comparison of non-integrating reprogramming methods. *Nat Biotechnol.* 2015;33:58–63. DOI: 10.1038/nbt.3070.
109. Suhr ST, Chang EA, Tjong J, et al. Mitochondrial rejuvenation after induced pluripotency. *PLoS One.* 2010;5:e14095. DOI: 10.1371/journal.pone.0014095.
110. Qian T, Heaster TM, Houghtaling AR, et al. Label-free imaging for quality control of cardiomyocyte differentiation. *Nat Commun.* 2021;12:4580. DOI: 10.1038/s41467-021-24868-1.
111. Rodimova SA, Meleshina AV, Kalabusheva EP, et al. Metabolic activity and intracellular PH in induced pluripotent stem cells differentiating in dermal and epidermal directions. *Methods Appl Fluoresc.* 2019;7:044002. DOI: 10.1088/2050-6120/ab3b3d.
112. Meleshina AV, Dudenkova VV, Shirmanova MV, et al. Probing metabolic states of differentiating stem cells using two-photon FLIM. *Sci Rep.* 2016;6:21853. DOI: 10.1038/srep21853.
113. Hirano K, Namihira M. FAD influx enhances neuronal differentiation of human neural stem cells by facilitating nuclear localization of LSD1. *FEBS Open Bio.* 2017;7:1932–1942. DOI: 10.1002/2211-5463.12331.
114. Shakiba N, Fahmy A, Jayakumaran G, et al. Cell competition during reprogramming gives rise to dominant clones. *Science.* 2019;364:eaan0925. DOI: 10.1126/science.aan0925.
115. Elsafi Mabrouk MH, Goetzke R, Abagnale G, et al. The spatial self-organization within pluripotent stem cell colonies is continued in detaching aggregates. *Biomaterials.* 2022;282:121389. DOI: 10.1016/j.biomaterials.2022.121389.
116. Díaz-Díaz C, Fernandez de Manuel L, Jimenez-Carretero D, et al. Pluripotency surveillance by Myc-driven competitive elimination of differentiating cells. *Dev Cell.* 2017;42:585–599.e4. DOI: 10.1016/j.devcel.2017.08.011.
117. Ulman V, Maška M, Magnusson KEG, et al. An objective comparison of cell-tracking algorithms. *Nat Methods.* 2017;14:1141–1152. DOI: 10.1038/nmeth.4473.
118. Jiménez-Torres JA, Beebe DJ, Sung KE. A microfluidic method to mimic luminal structures in the tumor microenvironment. *Methods Mol Biol.* 2016;1458:59–69. DOI: 10.1007/978-1-4939-3801-8\_5.
119. Salick MR, Napiwocki BN, Sha J, et al. Micropattern width dependent sarcomere development in human ESC-derived cardiomyocytes. *Biomaterials.* 2014;35:4454–4464. DOI: 10.1016/j.biomaterials.2014.02.001.
120. Walsh AJ, Cook RS, Manning HC, et al. Optical metabolic imaging identifies glycolytic levels, subtypes, and early-treatment response in breast cancer. *Cancer Res.* 2013;73:6164–6174. DOI: 10.1158/0008-5472.CAN-13-0527.
121. Walsh AJ, Skala MC. Optical metabolic imaging quantifies heterogeneous cell populations. *Biomed Opt Express.* 2015;6:559–573.
122. Holmes A, Donkin A, Witten IH. WEKA: a machine learning workbench. In: *Proceedings of ANZILS'94—Australian New Zealand Intelligent Information Systems Conference.* Brisbane, Australia: IEEE. 1994; pp. 357–361. DOI: 10.1109/ANZILS.1994.396988.
123. Arsham MS, Barch MJ, Lawce HJ. *The AGT Cytogenetics Laboratory Manual.* 4th ed. Hoboken, NJ: John Wiley & Sons, 2017.
124. Gonzalez Garcia JR, Meza-Espinoza JP, Massey GV, et al. Use of the International System for Human Cytogenetic Nomenclature (ISCN). *Blood.* 2006;108:3952–3953. DOI: 10.1182/blood-2006-06-031351.

Received: January 5, 2022  
 Accepted: March 28, 2022  
 Issue Publication Date: April 20, 2022